Computational Texture Analysis
The MTEX Project

Helmut Schaeben

Geoscience Mathematics and Informatics
Technische Universität Bergakademie Freiberg, Germany

AGH Krakòw, June 14-18, 2010

Short Course Texture Analysis with MTEX

Schedule of Short Course
"Texture Analysis with MTEX emphasizing EBSD Data Analysis"

Helmut Schaeben and Florian Bachmann
Geoscience Mathematics and Informatics
TU Bergakademie Freiberg, Germany

	Jun 14, 2010	Jun 15, 2010	Jun 16, 2010	Jun 17, 2010	Jun 18, 2010
9.00 am	**Lecture** Introduction to texture analysis	**Lecture** Rotations	**Lecture** Orientation density function, pole point plots, pole density function	**Lecture** Orientation statistics	**Exercise with PC** Practical project I
	Coffee break	Coffee break	Coffee break	Coffee break	Coffee break
11.00 am	**Lecture** Introduction to mathematical texture analysis	**Lecture** Crystallograhic orientations	**Lecture** Grain modeling	**Lecture** Radon transform on SO(3) and application to texture analysis	**Exercise with PC** Practical project II
	Lunch break	Lunch break	Lunch break	Lunch break	Lunch break
2.00 pm	**Exercise with PC** Introduction to MATLAB I	**Exercise with PC** Introduction to MTEX	**Exercise with PC** EBSD data analysis with MTEX I	**Exercise with PC** Texture analysis with MTEX I	**Exercise with PC** Practical project III
	Coffee break	Coffee break	Coffee break	Coffee break	Coffee break
4.00 pm	**Exercise with PC** Introduction to MATLAB II	**Exercise with PC** First steps with MTEX	**Exercise with PC** EBSD data analysis with MTEX II	**Exercise with PC** Texture analysis with MTEX II	**Exercise with PC** Practical project IV

The MTEX Project

Texture Analysis

Motivation

Texture Analysis – Analysis of Crystallographic Preferred Orientation

Crystallographic orientation is the rotational state of a coordinate system fixed to an individual crystal with respect to a coordinate system fixed to the specimen .

Texture, i.e. the statistical distribution of crystallographic orientations, controlls the physical properties of polycrystalline materials.

Texture Analysis
Analysis of Crystallographic Preferred Orientation

Let $f : SO(3) \to \mathbb{R}_+$ be an orientation probability density function. Then

$$\mathcal{R}f(\mathbf{h},\mathbf{r}) = \frac{1}{2\pi}\int_{G(\mathbf{h},\mathbf{r})} f(\boldsymbol{g})d\boldsymbol{g} = \text{prob}\Big(\boldsymbol{g} \in G(\mathbf{h},\mathbf{r})\Big)$$

with fibres

$$G(\mathbf{h},\mathbf{r}) = \Big\{\boldsymbol{g} \in SO(3)\,|\,\boldsymbol{g}\mathbf{h} = \mathbf{r}, (\mathbf{h},\mathbf{r}) \in \mathbb{S}^2 \times \mathbb{S}^2\Big\}$$

is also the probability that $\boldsymbol{g}\mathbf{h}$ statistically coincides with $\mathbf{r}$.

Experimentally

$$\frac{1}{2}\Big(\mathcal{R}f(\mathbf{h},\mathbf{r}) + \mathcal{R}f(-\mathbf{h},\mathbf{r})\Big)$$

is accessible with X–ray or neutron diffraction with a texture goniometer.

Applications of Texture Analysis: Materials Sciences

In materials sciences, texture analysis typically addresses problems like what pattern of crystallographic preferred orientation is caused by a given process, and refers to process control in the laboratory or quality control in production to guarantee a required crystallographic preferred orientation and corresponding macroscopic physical properties.

- isotropic steel – almost perfect uniform distribution, no crystallographic preferred orientation
- high–temperature semi–conductors – almost perfect “single crystal” crystallographic preferred orientation

Materials Sciences – Isotropic Steel

Applications of Texture Analysis: Geosciences

In geosciences, texture analysis is typically applied to the much more difficult problem of which process(es) caused an observed pattern of crystallographic preferred orientation in rocks and aims at an interpretation of the kinematics and dynamics of geological processes contributing to a consistent reconstruction of the geological deformation history.

- differences in the velocity of seismic waves along or across ocean ridges have recently been explained with textures changes during mantle convection
- varying texture may result in a seismic reflector
- texture of marble slabs employed as building facades or tombstone decoration is thought to significantly influence the spectacular phenomena of bending, fracturing, spalling and shattering of the initially intact slab

Applications of Texture Analysis: Geosciences

Paris Cimetiere Montparnasse

Die beiden aus porösen Tertiärkalkstein Calciere grossier gefertigten Stelen in der Bildmitte sind deutlich verbogen und weisen Rissphänomene auf.

Courtesy Prof. S. Siegesmund, Göttingen

Applications of Texture Analysis: Geosciences

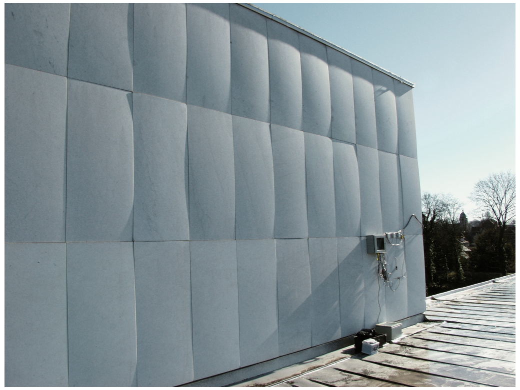

Helsinki, Finnlandia Halle

Riesige Fassadenflächen aus Carrara–Marmor zeigen deutliche "Einschüsselungen" (Verbiegungen).

Courtesy Prof. S. Siegesmund, Göttingen

The **MTEX** Project

Texture analysis –
Analysis of crystallographic preferred orientation

Texture analysis – Analysis of crystallographic preferred orientation

Objective of mathematical texture analysis: **Sander's vision**

Numerical determination of an orientation probability density function,

1. which explains experimental integral pole intensity data, or
2. which is derived from individual orientation measurements,

and its characteristics like

- harmonic (Fourier) coefficients, physical properties, ...
- texture index, entropy, ...
- modes, volume fractions around peaks or fibres
- grain boundaries, classification of grain boundaries, ...
- grain size distribution
- misorientation distribution
- ...

Experimental data

Integral pole intensity data

Superpositions of

$$\mathcal{R}f(\mathbf{h}_i, \mathbf{r}_{ij_i}) = \frac{1}{2\pi} \int_{\{g \in \mathrm{SO}(3) | g\mathbf{h}_i = \mathbf{r}_{ij_i}\}} f(g) dg$$

with symmetrically equivalent $\mathbf{h}_i \in \mathbb{S}^2$, where the determination of the unknown orientation density function $f : \mathrm{SO}(3) \to \mathbb{R}$ requires the resolution of an ill–posed inverse problem.

Individual orientation measurements

Spatially indexed orientations

$$g(x_i) = g_i \in \mathrm{SO}(3), x_i \in D \subset \mathbb{R}^d, i = 1, \ldots, n, \ d = 2, 3$$

give rise to non–parametric kernel density estimation of f.

Pole figures and orientation density function
The Radon transform on SO(3)

Integral Orientation measurements: Pole figure data

Orientation density function and its Radon transform

Let $f : \mathrm{SO}(3) \to [0, \infty)$ be a probability density function of a random rotation $g \in \mathrm{SO}(3)$.

Totally geodesic Radon transform

The one–dimensional *totally geodesic Radon transform* of f is defined as

$$\mathcal{R}f(\mathbf{h}, \mathbf{r}) = \frac{1}{2\pi} \int_{G(\mathbf{h},\mathbf{r})} f(g) dg, \ \ (\mathbf{h}, \mathbf{r}) \in \mathbb{S}^2 \times \mathbb{S}^2$$

with geodesics (“fibres”)

$$G(\mathbf{h}, \mathbf{r}) = \{g \in \mathrm{SO}(3) \,|\, g\,\mathbf{h} = \mathbf{r}, \ \ (\mathbf{h}, \mathbf{r}) \in \mathbb{S}^2 \times \mathbb{S}^2\}$$

It associates to an orientation probability density function f its mean values along the one–dimensional geodesics $G(\mathbf{h}, \mathbf{r})$.

Pole density, orientation density function

Basic crystallographic X–ray transform ...

The mean

$$P(\mathbf{h}, \mathbf{r}) = \frac{1}{2}\Big(\mathcal{R}f(\mathbf{h}, \mathbf{r}) + \mathcal{R}f(\mathbf{h}, -\mathbf{r})\Big) = \mathcal{X}f(\mathbf{h}, \mathbf{r}),$$

is experimentally accessible with diffraction and called *basic crystallographic X–ray transform* even though it does not depend on the radiation used for diffraction.

... without inverse

While the Radon transform possess a unique inverse under mild mathematical assumptions, the basic crystallographic X–ray transform does not.
Additional modeling assumptions are required to resolve the corresponding inversion probem.

Ambiguity

Two different ODFs

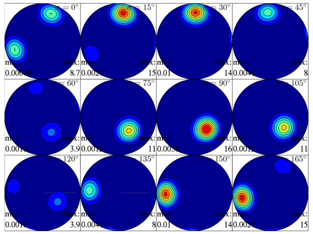

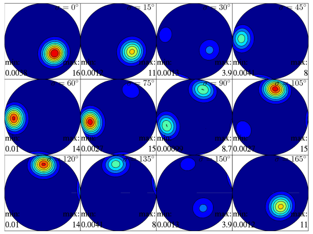

and their corresponding PDFs, respectively

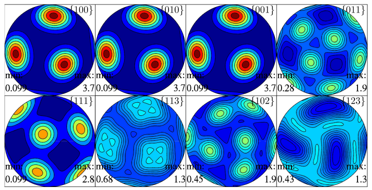

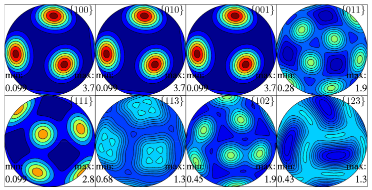

Pole density, orientation density function

Crystallographic X–ray transform

Eventually, we are interested in superpositions

$$\sum_{\mathbf{h} \in H_i} \rho_{\mathbf{h}} \mathcal{R} f(\mathbf{h}, \mathbf{r}) = \mathcal{R} f(H_i, \mathbf{r})$$

where $H_i = H(\lambda_i, \theta_i)$ is a set of superimposing crystal directions, and $\rho_{\mathbf{h}}, \mathbf{h} \in H_i$ are the relative reflection intensities.

Resolution of the practical inversion problem (1)

Darboux pde governing pole density functions

The general solution (Nikolayev and Schaeben, 1999) of the Darboux differential equation

$$\left(\Delta_{\mathbf{h}} - \Delta_{\mathbf{r}}\right) P(\mathbf{h}, \mathbf{r}) = 0$$

suggests two ways to tackle the practical inversion problem:

Alternatives

- harmonic analysis, i.e., Fourier series expansion, well localizable in frequency domain,
- radially symmetric basis functions, well localizable in spatial domain,

or a compromise of the two:

Resolution of the practical inversion problem (2)

Compromise

Functions which are well localized in both domains, more specifically functions which are radially symmetric in spatial domain and with Fourier coefficients which vanish smoothly and sufficiently fast.

Numerically

Radially symmetric basis functions approximated with finite harmonic series expansions applying fast Fourier techniques.

MTEX

This compromise is the core of the MATLAB toolbox **MTEX** .

Localization in frequency or spatial domain

While the spherical harmonics refer to localization in **frequency** domain, radial basis functions refer to localization in **spatial** domain.

frequency domain

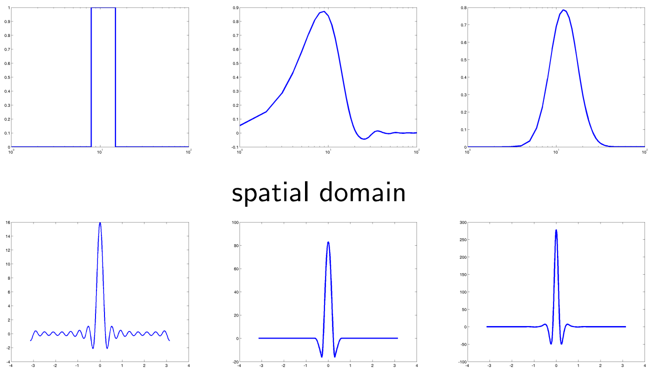

Examples of radially symmetric "wavelets" on the sphere

Examples of radially symmetric functions

de la Vallée Poussin

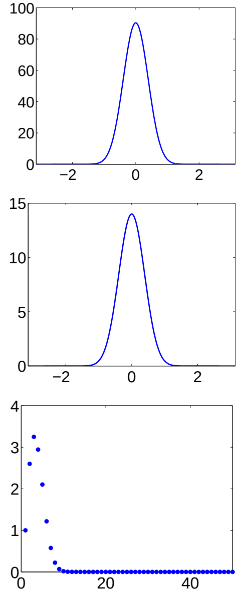

de la Vallée Poussin kernel

$$\psi_\kappa(\omega(gg_0^{-1})) = \frac{B(\frac{3}{2},\frac{1}{2})}{B(\frac{3}{2},\kappa+\frac{1}{2})} \cos^{2\kappa}\frac{\omega(gg_0^{-1})}{2},$$

$$\mathcal{R}\psi_\kappa(\mathbf{h},\mathbf{r}) = (1+\kappa)\cos^{2\kappa}\frac{\arccos(g_0\mathbf{h}\cdot\mathbf{r})}{2}$$

von Mises–Fisher

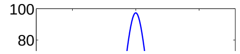

von Mises–Fisher kernel

Resolution of the practical inversion problem

Ansatz

We apply the model assumption that there are non–negative coefficients $\mathbf{c}$ such that

$$f(g) \approx \sum_{m=1}^{M} c_m\,\psi_\kappa(\omega(g\,g_m^{-1})).$$

Numerical resolution

Then we numerically solve the non–linear minimization problem

$$\hat{\mathbf{c}} = \operatorname{argmin} \sum_{i=1}^{N}\sum_{j_i=1}^{N_i} \frac{\left(\sum_{m=1}^{M} a(\mathbf{h}_i)\,c_m\,\mathcal{X}\psi_\kappa(g_m\mathbf{h}_i,\mathbf{r}_{j_i}) + I_{ij_i}^b - \mathbf{I}_{ij_i}\right)^2}{\mathbf{I}_{ij_i}}$$
$$+\lambda\left\|\sum_{m=1}^{M} c_m\,\psi_\kappa(\circ\,g_m^{-1})\right\|^2_{\mathcal{H}(\mathrm{SO}(3))},$$

where λ is the parameter of regularization weighting the penalty term.

EBSD data and orientation density function

Individual Orientation measurements: EBSD data

Kernel density estimation with individual orientation measurements (EBSD)

Kernel density estimator and its Radon transform

Let $g(x_i) = g_i \in SO(3), x_i \in D \subset \mathbb{R}^d, i = 1, \ldots, n, d = 2, 3$, be individual orientation measurements, and let $\psi_\kappa(\omega(g\, g_0^{-1}))$ be a kernel, i.e., a non–negative, radially symmetric bell–shaped function on SO(3) well localized around its center $g_0 \in SO(3)$, with a parameter κ controling its spatial localization.

Then the kernel density estimator is

$$f^*_\kappa(g; g_1, \ldots, g_n) = \frac{1}{n} \sum_{i=1}^{n} \psi_\kappa(\omega(g\, g_i^{-1})).$$

and its Radon transform

$$\mathcal{R}[f^*_\kappa(\circ; g_1, \ldots, g_n)](\mathbf{h}, \mathbf{r}) = \frac{1}{n} \sum_{i=1}^{n} \mathcal{R}\psi_\kappa(g_i \mathbf{h} \cdot \mathbf{r})\,.$$

The MTEX Project

References

References (1)

Hielscher, R., Schaeben, H., Siemes, H., 2010, Orientation distribution within a single hematite crystal: Mathematical Geosciences 42, 359-375

Bachmann, F., Hielscher, R., Schaeben, H., 2010, Texture Analysis with MTEX Free and Open Source Software Toolbox: Solid State Phenomena 160, 63-68

Hielscher, R., Schaeben, H., 2008, A novel pole figure inversion method: Specification of the MTEX algorithm: J. Appl. Cryst. 41, 1024-1037

References (2)

Bernstein, S., Hielscher, R., Schaeben, H., 2009, The generalized totally geodesic Radon transform and its application to texture analysis: Mathematical Methods in the Applied Sciences 32, 379-394

Hielscher, R., Potts, D., Prestin, J., Schaeben, H., Schmalz, M., 2008, The Radon transform on SO(3): A Fourier slice theorem and numerical inversion: Inverse Problems 24, 025011 (21p)

Boogaart, K.G.v.d., Hielscher, R., Prestin, J., Schaeben, H., 2007, Kernel-based methods for inversion of the Radon transform on SO(3) and their applications to texture analysis: Journal of Computational and Applied Mathematics 199, 122-140

Bernstein, S., Schaeben, H., 2005, A one-dimensional Radon transform on SO(3) and its application to texture goniometry: Mathematical Methods in the Applied Sciences 28, 1269-1289

References (2)

Meister, L., Schaeben, H., 2004, A concise quaternion geometry of rotations: Mathematical Methods in the Applied Sciences 28, 101-126

Kunze, K., Schaeben, H., 2004, The Bingham distribution of rotations and its spherical Radon transform in texture analysis: Mathematical Geology 36, 917-943

Nikolayev, D.I., Schaeben, H., 1999, Characteristics of the ultrahyperbolic differential equation governing pole density functions: Inverse Problems 15, 1603-1619

The MTEX Project

Ill–Posedness

Ill-Posedness

The reference is

Tikhonov, A.N. and Arsenin, V.Y., 1977, *Solutions of Ill - Posed Problems*: J. Wiley & Sons, New York

Ill-Posedness (1)

A classic example (Tikhonov) is

$$\begin{aligned} 10x + y &= 11 \\ 100x + 11y &= 111 \end{aligned}$$

with the unique and exact solution $x = 1, y = 1$, and

$$\begin{aligned} 10x + y &= 11,1 \\ 100x + 11y &= 111 \end{aligned}$$

with the unique and exact solution $x = 1.11, \;\; y = 0$

Ill-Posedness (2)

Slight modifications result in an even worse conditioned system

$$\begin{aligned} x + 10y &= 11 \\ 10x + 101y &= 111 \end{aligned}$$

with the unique and exact solution $x = 1, y = 1$,
and

$$\begin{aligned} x + 10y &= 11,1 \\ 10x + 101y &= 111 \end{aligned}$$

with the unique and exact solution $x = 11.1, \;\; y = 0$

Ill-Posedness (3)

Another very simple yet instructive example of ill-posedness may be provided by the following two systems of linear equations

$$\begin{aligned} x + 0.999y &= 1 \\ x + y &= 0 \end{aligned}$$

with the unique and exact solution $x = 1000, \;\; y = -1000$,
and

$$\begin{aligned} x + 1.001y &= 1 \\ x + y &= 0 \end{aligned}$$

with the unique and exact solution $x = -1000, y = +1000$. Though the matrices of the two systems differ in only one entry, and these two entries differ only by .002, the solutions differ drastically.

The **MTEX** Project

Rotations

Definition of a rotation

A (proper) rotation $\boldsymbol{g} : \mathbb{R}^3 \mapsto \mathbb{R}^3$ is a linear mapping preserving handedness of a set of vectors (later: det $M(\boldsymbol{g}) = 1$), and the scalar product of vectors, i.e. the angle of vectors, which is the canonical measure of distance of unit vectors, i.e. on the sphere $\mathbb{S}^2 \subset \mathbb{R}^3$.

Issues

- parametrization of a rotation – mathematical “quantitative” description of a rotation
- embedding of a rotation – to perform a rotation
- visualization of a set of rotations – exploratory data analysis

Parametrizations and Embeddings of Rotations

Parametrizations of a rotation

Basic parametrizations to quantitatively describe a rotation are

- angle $\omega \in [0, \pi]$ and axis $\mathbf{n} \in \mathbb{S}^2$ of rotation *(why not $\omega \in [0, 2\pi)$)*,
- three Euler angles (α, β, γ), $\alpha, \gamma \in [0, 2\pi)$, $\beta \in [0, \pi]$ with respect to three orthogonal axes of three successive rotations
- ...

Representations of a rotation

Basic embeddings to perform a rotation are

- matrix embedding
- quaternion embedding
- Rodrigues' embedding
- harmonic representation
- ...

Parametrizations and embeddings of a rotation (1)

- angle $\omega \in [0, \pi]$ and axis $\mathbf{n} \in \mathbb{S}^2 \subset \mathbb{R}^3$ of rotation:

$$\boldsymbol{g} = \boldsymbol{g}(\omega, \mathbf{n}), \quad M(\boldsymbol{g}) = M_{ij}(\omega, \mathbf{n}))_{i,j=1,2,3}$$

  which may be rewritten as

$$\boldsymbol{g} = \boldsymbol{g}(\omega\mathbf{n}), \quad M(\boldsymbol{g}) = M_{ij}(\omega\mathbf{n}))_{i,j=1,2,3}$$

  What is the difference?
- quaternions $\mathbf{q} \in S^3_+ \subset \mathbb{R}^4$:

$$q(\boldsymbol{g}) = \cos\omega/2 + \mathbf{n}\sin\omega/2$$

  Note: Quaternion multiplication applies.
- Rodrigues' embedding $\mathbf{R} \in \mathbb{R}^3$:

$$\mathbf{R}(\boldsymbol{g}) = \mathbf{n}\tan\omega/2$$

Parametrizations and embeddings of a rotation (2)

- Euler angles $(\alpha, \beta, \gamma) \in [0, 2\pi] \times [0, \pi] \times [0, 2\pi]$ of 3 successive rotations around (conventionally) fixed axes of rotations:

$$\boldsymbol{g} = \boldsymbol{g}(\alpha, \beta, \gamma), \;\; M(\boldsymbol{g}) = M_{ij}(\alpha, \beta, \gamma))_{i,j=1,2,3}$$

There exist 12 essentially different ways to define Euler angles, and they are all in use, somewhere (Kuipers, 1999).

Parametrization of the inverse rotation in terms of angle and axis of a rotation

If a rotation $\boldsymbol{g}$ is parametrized in terms of its angle ω and its axis $\mathbf{n} \in \mathbb{S}^2$, then the inverse rotation $\boldsymbol{g}^{-1}$ is parametrized by $(\omega, -\mathbf{n})$. *Why is it not parametrized by* $(2\pi - \omega, \mathbf{n})$*?*

If a rotation $\boldsymbol{g}$ is represented by a (3×3) matrix $M \in \mathbf{SO}(3)$, then the inverse rotation $\boldsymbol{g}^{-1}$ is represented by $M^{-1} = M^t$.

Conjugation of a rotation

Let $\boldsymbol{g}_0$ be an arbitrary rotation, and let $\boldsymbol{g}$ be a rotation parametrized by its angle ω and axis $\mathbf{n}$. The the sequence $\boldsymbol{g}_0 \boldsymbol{g} \boldsymbol{g}_0^{-1}$ of three successive rotations is called conjugation of $\boldsymbol{g}$ by $\boldsymbol{g}_0$, and is parametrized by its angle ω and axis $\boldsymbol{g}_0 \, \mathbf{n}$, i.e.

$$\boldsymbol{g}_0 \, \boldsymbol{g}(\omega, \mathbf{n}) \, \boldsymbol{g}_0^{-1} = \boldsymbol{g}(\omega, \boldsymbol{g}_0 \, \mathbf{n})$$

In particular, a rotation and any of its conjugate have the same angle of rotation.

Matrix embedding in terms of angle and axis of a rotation

In terms of the (angle, axis) – parametrization, the rotation $\boldsymbol{g}(\omega, \mathbf{n})$ has the matrix embedding

$$M(\boldsymbol{g}(\omega, \mathbf{n})) = \begin{pmatrix} n_1^2(1 - \cos\omega) + \cos\omega & n_1 n_2(1 - \cos\omega) - n_3 \sin\omega & n_1 n_3(1 - \cos\omega) + n_2 \sin\omega \\ n_1 n_2(1 - \cos\omega) + n_3 \sin\omega & n_2^2(1 - \cos\omega) + \cos\omega & n_2 n_3(1 - \cos\omega) - n_1 \sin\omega \\ n_1 n_3(1 - \cos\omega) - n_2 \sin\omega & n_2 n_3(1 - \cos\omega) + n_1 \sin\omega & n_3^2(1 - \cos\omega) + \cos\omega \end{pmatrix}$$

$$= \begin{pmatrix} 1 - 2(n_2^2 + n_3^2)\sin^2\frac{\omega}{2} & -n_3 \sin\omega + 2n_1 n_2 \sin^2\frac{\omega}{2} & n_2 \sin\omega + 2n_1 n_3 \sin^2\frac{\omega}{2} \\ n_3 \sin\omega + 2n_1 n_2 \sin^2\frac{\omega}{2} & 1 - 2(n_1^2 + n_3^2)\sin^2\frac{\omega}{2} & -n_1 \sin\omega + 2n_2 n_3 \sin^2\frac{\omega}{2} \\ -n_2 \sin\omega 2 + 2n_1 n_3 \sin^2\frac{\omega}{2} & n_1 \sin\omega + 2n_2 n_3 \sin^2\frac{\omega}{2} & 1 - 2(n_1^2 + n_2^2)\sin^2\frac{\omega}{2} \end{pmatrix}$$

Euler angles (1)

Euler's Theorem states that any two orthonormal coordinate systems can be related by a sequence of rotations (not more than three) about coordinate axes, where two successive rotations must not be about the same axis.

Any rotation $\boldsymbol{g}$ can be represented as a sequence of three successive rotations about conventionally specified coordinate axes by three corresponding "Euler" angles.

There exist twelve choices of sets of axes of rotations (in terms of the coordinate axes of the initial coordinate system) to define correponding Euler angles, and they are all in use, somewhere.

Euler angles (2)

Bunge's Euler angles $(\varphi_1, \phi, \varphi_2)$ of 3 successive rotations around (conventionally) fixed axes of rotations:

- the first rotation by $\varphi_1 \in [0, 2\pi)$ about the **z**–axis,
- the second by $\phi \in [0, \pi]$ about the *new* **x**–axis,
- the third by $\varphi_2 \in [0, 2\pi)$ about the *new* **z**–axis.

$$\boldsymbol{g}_{\mathrm{HJB}}(\varphi_1, \phi, \varphi_2) := \boldsymbol{g}(\varphi_2, \mathbf{z}'')\,\boldsymbol{g}(\phi, \mathbf{x}')\,\boldsymbol{g}(\varphi_1, \mathbf{z})$$

Euler angles (3)

Roe's, Matthies' Euler angles (α, β, γ) of 3 successive rotations around (conventionally) fixed axes of rotations:

- the first rotation by $\alpha \in [0, 2\pi)$ about the **z**–axis,
- the second by $\beta \in [0, \pi]$ about the *new* **y**–axis,
- the third by $\gamma \in [0, 2\pi)$ about the *new* **z**–axis.

$$\boldsymbol{g}_{\mathrm{SM}}(\alpha, \beta, \gamma) := \boldsymbol{g}(\gamma, \mathbf{z}'')\,\boldsymbol{g}(\beta, \mathbf{y}')\,\boldsymbol{g}(\alpha; \mathbf{z})$$

Then (α, β) are the spherical coordinates of the crystal direction $\mathbf{z}_{K_{\mathcal{C}}} = \mathbf{c}$ with respect to $K_{\mathcal{S}}$.

Euler angles (4)

Outside the texture universe, Euler angles (α, β, γ) usually define a rotation $\boldsymbol{g}$ in terms of a sequence $\boldsymbol{g}(\alpha,\, \beta,\, \gamma)$ of 3 successive rotations $\boldsymbol{g}(\alpha,\, \mathbf{z})\,\boldsymbol{g}(\beta,\, \mathbf{y})\,\boldsymbol{g}(\gamma,\, \mathbf{z})$ around (conventionally) fixed axes of rotations:

- the first rotation by $\gamma \in [0, 2\pi)$ about the **z**–axis,
- the second by $\beta \in [0, \pi]$ about the (initial) **y**–axis,
- the third by $\alpha \in [0, 2\pi)$ about the (initial) **z**–axis

of the specimen coordinate system $K_{\mathcal{S}}$,

$$\boldsymbol{g}(\alpha,\, \beta,\, \gamma) := \boldsymbol{g}(\alpha, \mathbf{z})\,\boldsymbol{g}(\beta, \mathbf{y})\,\boldsymbol{g}(\gamma, \mathbf{z})$$

Euler angles (5)

The differently defined Euler angles are related by

$$\begin{aligned}
\boldsymbol{g}(\alpha,\beta,\gamma) &= \boldsymbol{g}(\alpha,\mathbf{z})\,\boldsymbol{g}(\beta,\mathbf{y})\,\boldsymbol{g}(\gamma,\mathbf{z}) \\
&= \underbrace{\boldsymbol{g}(\alpha,\mathbf{z})\boldsymbol{g}(\beta,\mathbf{y})\boldsymbol{g}^{-1}(\alpha,\mathbf{z})}_{\boldsymbol{g}(\beta,[\boldsymbol{g}(\alpha,\mathbf{z})\mathbf{y}])=\boldsymbol{g}(\beta,\mathbf{y}')}\;\underbrace{\boldsymbol{g}(\alpha,\mathbf{z})\boldsymbol{g}(\gamma,\mathbf{z})\boldsymbol{g}^{-1}(\alpha,\mathbf{z})}_{\boldsymbol{g}(\gamma,\mathbf{z})}\;\boldsymbol{g}(\alpha,\mathbf{z}) \\
&= \underbrace{\boldsymbol{g}(\beta,\mathbf{y}')\boldsymbol{g}(\gamma,\mathbf{z})\boldsymbol{g}^{-1}(\beta,\mathbf{y}')}_{\boldsymbol{g}(\gamma,[\boldsymbol{g}(\beta,\mathbf{y}')\mathbf{z}])}\;\boldsymbol{g}(\beta,\mathbf{y}')\,\boldsymbol{g}(\alpha,\mathbf{z}) \\
&= \boldsymbol{g}(\gamma,\mathbf{z}'')\,\boldsymbol{g}(\beta,\mathbf{y}')\,\boldsymbol{g}(\alpha,\mathbf{z}) = \boldsymbol{g}_{\mathsf{SM}}(\alpha,\beta,\gamma)
\end{aligned}$$

Euler angles (6)

Let $\mathbf{a},\mathbf{b},\mathbf{c}$ denote the right–handed coordinate axes of the rotated coordinate system $K_{\mathcal{C}}$. When considering $\mathbf{x},\mathbf{y},\mathbf{z}$ in terms of (rotated) $\mathbf{a},\mathbf{b},\mathbf{c}$, then of course

$$\begin{aligned}
\boldsymbol{g}(\alpha,\mathbf{z})\,\boldsymbol{g}(\beta,\mathbf{y})\,\boldsymbol{g}(\gamma,\mathbf{z}) &= \boldsymbol{g}(\gamma,\mathbf{z}'')\,\boldsymbol{g}(\beta,\mathbf{y}')\,\boldsymbol{g}(\alpha,\mathbf{z}) \\
&= \boldsymbol{g}(\gamma,\mathbf{c})\,\boldsymbol{g}(\beta,\mathbf{b}')\,\boldsymbol{g}(\alpha,\mathbf{c}'') \\
&= \boldsymbol{g}(\alpha,\mathbf{c})\,\boldsymbol{g}(\beta,\mathbf{b})\,\boldsymbol{g}(\gamma,\mathbf{c})
\end{aligned}$$

and

$$\boldsymbol{g}(-\alpha,\mathbf{c}'')\,\boldsymbol{g}(-\beta,\mathbf{b}')\,\boldsymbol{g}(-\gamma,\mathbf{c}) = \boldsymbol{g}(-\gamma,\mathbf{c})\,\boldsymbol{g}(-\beta,\mathbf{b})\,\boldsymbol{g}(-\alpha,\mathbf{c})$$

Matrix embedding in terms of Euler angles (1)

$$M(\boldsymbol{g}(\gamma,\mathbf{z})) = \begin{pmatrix} \cos\gamma & -\sin\gamma & 0 \\ \sin\gamma & \cos\gamma & 0 \\ 0 & 0 & 1 \end{pmatrix}$$

$$M(\boldsymbol{g}(\beta,\mathbf{y})) = \begin{pmatrix} \cos\beta & 0 & \sin\beta \\ 0 & 1 & 0 \\ -\sin\beta & 0 & \cos\beta \end{pmatrix}$$

$$M(\boldsymbol{g}(\alpha,\mathbf{z})) = \begin{pmatrix} \cos\alpha & -\sin\alpha & 0 \\ \sin\alpha & \cos\alpha & 0 \\ 0 & 0 & 1 \end{pmatrix}$$

Matrix embedding in terms of Euler angles (2)

$$\begin{aligned}
M(\boldsymbol{g}(\alpha,\beta,\gamma)) &= \begin{pmatrix} \cos\alpha & -\sin\alpha & 0 \\ \sin\alpha & \cos\alpha & 0 \\ 0 & 0 & 1 \end{pmatrix}\begin{pmatrix} \cos\beta & 0 & \sin\beta \\ 0 & 1 & 0 \\ -\sin\beta & 0 & \cos\beta \end{pmatrix}\begin{pmatrix} \cos\gamma & -\sin\gamma & 0 \\ \sin\gamma & \cos\gamma & 0 \\ 0 & 0 & 1 \end{pmatrix} \\
&= \begin{pmatrix} \cos\alpha\cos\beta\cos\gamma - \sin\alpha\sin\gamma & -\cos\alpha\cos\beta\sin\gamma - \sin\alpha\cos\gamma & \cos\alpha\sin\beta \\ \sin\alpha\cos\beta\cos\gamma + \cos\alpha\sin\gamma & -\sin\alpha\cos\beta\sin\gamma + \cos\alpha\cos\gamma & \sin\alpha\sin\beta \\ -\sin\beta\cos\gamma & \sin\beta\sin\gamma & \cos\beta \end{pmatrix}
\end{aligned}$$

Parametrization ot the inverse rotation in terms of Euler angles

If $\boldsymbol{g} = \boldsymbol{g}(\alpha, \beta, \gamma)$, then the inverse rotation in terms of Matthies'/Bunge's Euler angles is formally parametrized by

$$\boldsymbol{g}^{-1} = \boldsymbol{g}(-\gamma, -\beta, -\alpha) = \boldsymbol{g}(\pi - \gamma, \beta, \pi - \alpha)$$

or

$$\boldsymbol{g}^{-1} = \boldsymbol{g}(-\varphi_2, -\phi, -\varphi_1),$$

resp.

Of course, the matrix embedding of the inverse rotation $\boldsymbol{g}^{-1}$ is the transposed matrix of the initial rotation $\boldsymbol{g}$, i.e.

$$M(\boldsymbol{g}^{-1}) = M^{-1}(\boldsymbol{g}) = M^{t}(\boldsymbol{g})$$

The MTEX Project

Geometry of Rotations

Contents

1. **Motivation**
2. **Definition and Basic Properties of Quaternions**
3. **Geometry of Rotations**
4. **Radon Transforms on SO(3)**

Historical Notes

- $\mathbb{N}$, $\mathbb{Z}$, $\mathbb{Q}$, $\mathbb{R}$, $\mathbb{R}^d$, $\mathbb{C}$, ...
- Given two rotations $\boldsymbol{g}_1, \boldsymbol{g}_2$ in terms of their axis and angle of rotation, what is the axis and the angle of the composed rotation $\boldsymbol{g}_2\boldsymbol{g}_1$?

The answer to both problems is provided by the skew field $\mathbb{H}$ of real quaternions.

Motivation

Texture Analysis – Analysis of Crystallographic Preferred Orientation

Crystallographic orientation is the rotational state of a coordinate system fixed to an individual crystal with respect to a coordinate system fixed to the specimen .

Texture, i.e. the statistical distribution of crystallographic orientations, controlls the physical properties of polycrystalline materials.

Texture Analysis
Analysis of Crystallographic Preferred Orientation

Let $f : SO(3) \to \mathbb{R}_+$ be an orientation probability density function. Then

$$\mathcal{R}f(\mathbf{h},\mathbf{r}) = \frac{1}{2\pi}\int_{G(\mathbf{h},\mathbf{r})} f(\boldsymbol{g})d\boldsymbol{g} = \operatorname{prob}\Big(\boldsymbol{g} \in G(\mathbf{h},\mathbf{r})\Big)$$

with fibres

$$G(\mathbf{h},\mathbf{r}) = \Big\{\boldsymbol{g} \in SO(3)\,|\,\boldsymbol{g}\mathbf{h} = \mathbf{r}, (\mathbf{h},\mathbf{r}) \in \mathbb{S}^2 \times \mathbb{S}^2\Big\}$$

is also the probability that $\boldsymbol{g}\mathbf{h}$ statistically coincides with $\mathbf{r}$.

Experimentally

$$\frac{1}{2}\Big(\mathcal{R}f(\mathbf{h},\mathbf{r}) + \mathcal{R}f(-\mathbf{h},\mathbf{r})\Big)$$

is accessible with X–ray or neutron diffraction with a texture goniometer.

Applications of Texture Analysis: Materials Sciences

In materials sciences, texture analysis typically addresses problems like what pattern of crystallographic preferred orientation is caused by a given process, and refers to process control in the laboratory or quality control in production to guarantee a required crystallographic preferred orientation and corresponding macroscopic physical properties.

- isotropic steel – almost perfect uniform distribution, no crystallographic preferred orientation
- high–temperature semi–conductors – almost perfect "single crystal" crystallographic preferred orientation

Materials Sciences – Isotropic Steel

Applications of Texture Analysis: Geosciences

In geosciences, texture analysis is typically applied to the much more difficult problem of which process(es) caused an observed pattern of crystallographic preferred orientation in rocks and aims at an interpretation of the kinematics and dynamics of geological processes contributing to a consistent reconstruction of the geological deformation history.

- differences in the velocity of seismic waves along or across ocean ridges have recently been explained with textures changes during mantle convection
- varying texture may result in a seismic reflector
- texture of marble slabs employed as building facades or tombstone decoration is thought to significantly influence the spectacular phenomena of bending, fracturing, spalling and shattering of the initially intact slab

Applications of Texture Analysis: Geosciences

Paris Cimetiere Montparnasse

Die beiden aus porösen Tertiärkalkstein Calciere grossier gefertigten Stelen in der Bildmitte sind deutlich verbogen und weisen Rissphänomene auf.

Courtesy Prof. S. Siegesmund, Göttingen

Applications of Texture Analysis: Geosciences

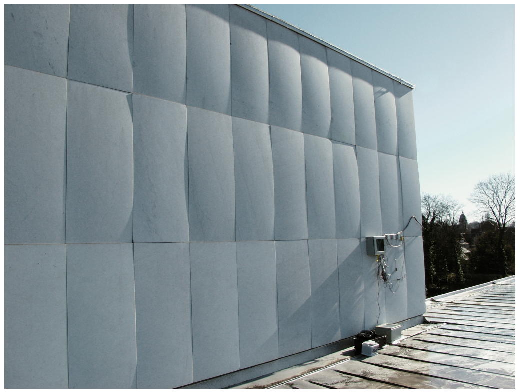

Helsinki, Finnlandia Halle

Riesige Fassadenflächen aus Carrara–Marmor zeigen deutliche "Einschüsselungen" (Verbiegungen).

Courtesy Prof. S. Siegesmund, Göttingen

Part I

Definition and Basic Properties of Quaternions

FIGURE 1.1 *Sir William Rowan Hamilton, 4 August 1805–2 September 1865.* (History of Mathematics web pages of the University of St. Andrews, Scotland.)

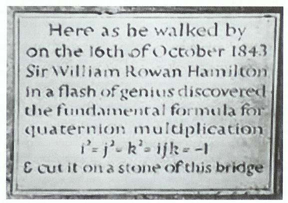

FIGURE 1.2 *The plaque on Broome Bridge in Dublin, Ireland, commemorating the legendary location where Hamilton conceived of the idea of quaternions. In fact, Hamilton and his wife were walking on the banks of the canal beneath the bridge, and the plaque is set in a wall there.* (Photograph courtesy University of Dublin.)

from: Andrew J. Hanson, Visualizing Quaternions: Elsevier, 2006

Skew–field of real quaternions (1)

An arbitrary quaternion $q \in \mathbb{H}$ is composed of its scalar and vector part

$$q = q_0 + iq_1 + jq_2 + kq_3 = q_0 + \mathbf{q} = \mathrm{Sc}q + \mathrm{Vec}q$$

with $\mathbf{q} = \mathrm{Vec}q$ and $q_0 = \mathrm{Sc}q$, where $\mathrm{Vec}q$ denotes the vector part of q, and $\mathrm{Sc}q$ denotes the scalar part of q.

The basis elements $1, i, j, k$ fulfil the algebraic relations

(i) $i^2 = j^2 = k^2 = -1$;

(ii) $ij = k, \quad jk = i, \quad ki = j$;

(iii) $ij + ji = jk + kj = ki + ik = 0$.

If $\mathrm{Sc}q = 0$, then q is called a pure quaternion, the subset of all pure quaternions is denoted $\mathrm{Vec}\mathbb{H}$. For $q \in \mathrm{Vec}\mathbb{H}$, q and $\mathbf{q}$ are identified, i.e. $q = \mathbf{q}$. The subset of all scalars may be denoted $\mathrm{Sc}\mathbb{H}$. In this way $\mathbb{R}$ and $\mathbb{R}^3$ are embedded in $\mathbb{H}$.

Skew–field of real quaternions (2)

Given two quaternions, $p, q \in \mathbb{H}$, their product according to the algebraic rules above is given by

$$pq = p_0 q_0 - \mathbf{p} \cdot \mathbf{q} + p_0 \mathbf{q} + q_0 \mathbf{p} + \mathbf{p} \times \mathbf{q} \ ,$$

where $\mathbf{p} \cdot \mathbf{q}$ and $\mathbf{p} \times \mathbf{q}$ represent the standard inner and wedge product in $\mathbb{R}^3$; thus

$$\begin{aligned} \mathrm{Sc}(pq) &= p_0 q_0 - \mathbf{p} \cdot \mathbf{q} \ , \\ \mathrm{Vec}(pq) &= p_0 \mathbf{q} + q_0 \mathbf{p} + \mathbf{p} \times \mathbf{q} \ . \end{aligned} \tag{1}$$

Conjugation of a real quaternion

The quaternion

$$q^* = \mathrm{Sc}q - \mathrm{Vec}q$$

is called the conjugate of q.

With conjugated quaternions it is possible to represent the scalar and vector part in an algebraic fashion as

$$\begin{aligned} q_0 &= \mathrm{Sc}q = \frac{1}{2}(q + q^*) \ , \\ \mathbf{q} &= \mathrm{Vec}q = \frac{1}{2}(q - q^*) \ . \end{aligned} \tag{2}$$

Norm of a real quaternion (1)

It holds that

$$qq^* = q^*q = \|q\|^2 = q_0^2 + (q^1)^2 + (q^2)^2 + (q^3)^2,$$

and the number $\| q \|$ is called the norm of q.

The norm of quaternions coincides with the Euclidean norm of q regarded as an element of the vector space $\mathbb{R}^4$.

The usual Euclidean inner product in the space $\mathbb{R}^4$ corresponds to the scalar part of pq^*, i.e. considering quaternions as vectors $\mathbf{p}, \mathbf{q} \in \mathbb{R}^4$, one gets

$$\mathbf{p} \cdot \mathbf{q} = \mathrm{Sc}(pq^*),$$

It holds that $(pq)^* = q^* p^*$, and therefore $\| pq \| = \| p \| \, \| q \|$.

Norm of a real quaternion (2)

A quaternion q with $\|q\| = 1$ is called a unit quaternion.

Furthermore, let $\mathbb{S}^2$ denote the unit sphere in $\mathrm{Vec}\,\mathbb{H} \simeq \mathbb{R}^3$ of all unit vectors, and $\mathbb{S}^3$ the sphere in $\mathbb{H} \simeq \mathbb{R}^4$ of all unit quaternions.

In complete analogy to $\mathbb{S}^3 \subset \mathbb{R}^4$, $\mathrm{Sc}(pq^*)$ provides a canonical measure for the spherical distance of unit quaternions $p, q \in \mathbb{S}^3$.

Inverse of a real quaternion

Moreover, each non-zero quaternion q has a unique inverse

$$q^{-1} = q^*/\|q\|^2.$$

with $\|q^{-1}\| = \|q\|^{-1}$.

For unit quaternions it is $q^{-1} = q^*$; for pure unit quaternions it is $q^{-1} = -q$, implying $qq = -1$.

Orthogonality of real quaternions

Definition

Two quaternions $p, q \in \mathbb{H}$ are said to be orthogonal if pq^* is a pure quaternion. If p, q are orthogonal unit quaternions, they are called orthonormal quaternions.

The condition of orthogonality means that $pq^* \in \mathrm{Vec}\mathbb{H}$, or according to Eq. (2)

$$2\,\mathrm{Sc}(pq^*) = pq^* + qp^* = 0.$$

It is emphasized that pure quaternions with orthogonal vector parts are orthogonal, but that the inverse is not generally true. Orthogonality of two quaternions does not imply orthogonality of their vector parts unless they are pure quaternions.

Representation of real quaternions

An arbitrary quaternion permits the representation

$$q = \|\, q \,\| \left(\frac{q_0}{\|q\|} + \frac{\mathbf{q}}{\|\,\mathbf{q}\,\|} \frac{\|\,\mathbf{q}\,\|}{\|q\|} \right) = \|\, q \,\| \left(\cos\frac{\omega}{2} + \frac{\mathbf{q}}{\|\,\mathbf{q}\,\|} \sin\frac{\omega}{2} \right)$$

with $\omega = 2\arccos(q_0/\|q\|)$, and $\|\,\mathbf{q}\,\|^2 = \mathbf{q}\mathbf{q}^*$ considering $\mathbf{q}$ as a pure quaternion.

For an arbitrary unit quaternion the representation

$$q = \cos\frac{\omega}{2} + \mathbf{n}\sin\frac{\omega}{2} \tag{3}$$

with the normalized vector part $\mathbf{n} = \mathbf{q}/\|\mathbf{q}\| \in \mathbb{S}^2$ will often be applied in the context of rotations, where $\mathbf{n} \in \mathbb{S}^2$ denotes the axis and ω the angle of a counter–clockwise rotation about $\mathbf{n}$.

Part II

Geometry of Rotations

Quaternion representation of rotations in $\mathbb{R}^3$ (1)

Any rotation $\boldsymbol{g}$ mapping the unit vector $\mathbf{h} \in \mathbb{S}^2$ onto the unit vector $\mathbf{r} \in \mathbb{S}^2$ according to

$$\boldsymbol{g}\,\mathbf{h} = \mathbf{r}$$

can be written in terms of its unit quaternion representation $q \in \mathbb{S}^3 \subset \mathbb{H}$ as

$$q(\boldsymbol{g})\,\mathbf{h}\,q^*(\boldsymbol{g}) = \mathbf{r}$$

where quaternion multiplication applies.

To perform quaternion multiplication, $\mathbf{h}$ and $\mathbf{r}$ must be read as pure quaternions, i.e. they must be augmented with a zero scalar quaternion part; then

$$q\,h\,q^* = r$$

It explicitly reads then

$$\mathbf{r} = \mathbf{h}\,\cos\omega + (\mathbf{n} \times \mathbf{h})\,\sin\omega + (\mathbf{n} \cdot \mathbf{h})\,\mathbf{n}\,(1 - \cos\omega) \tag{4}$$

where the representation of Eq. (3) has been applied.

Quaternion representation of rotations in $\mathbb{R}^3$ (3)

The unit quaternion $q \in \mathbb{S}^3$ represents the rotation about the axis $\mathbf{q}$ by the angle $\omega = 2\arccos(q_0)$. Therefore, each unit quaternion $q \in \mathbb{S}^3$ can be seen as a representation of a rotation in $\mathbb{R}^3$, i.e. $\mathbb{S}^3$ stands for a double covering of the group $SO(3)$.

It is emphasized that $\mathbb{S}^2 \subset \mathrm{Vec}\mathbb{H}$ consists of all quaternions representing rotations by the angle π about arbitrary axes, as every unit vector $\mathbf{q}$ can be considered as the pure quaternion $q = \cos(\pi/2) + \mathbf{q}\sin(\pi/2)$.

The unit quaternion q^* represents the inverse rotation $\boldsymbol{g}^{-1}\,\mathbf{r} = \mathbf{h}$.

Quaternion representation of rotations in $\mathbb{R}^3$ (4)

Proposition

Let $p, q \in \mathbb{S}^3$ be arbitrary unit quaternions, where q represents the rotation about the axis $\mathbf{n}$ by the angle ω according to Eq. (3). Then the quaternion $pqp^* \in \mathbb{S}^3$ represents the rotation about the rotated axes $p\,\mathbf{n}\,p^* \in \mathbb{S}^2$ by the same angle ω.

Proof. It simply holds that

$$pqp^* = p\Big(\cos\frac{\omega}{2} + \mathbf{n}\sin\frac{\omega}{2}\Big)p^* = \cos\frac{\omega}{2} + p\mathbf{n}p^*\sin\frac{\omega}{2} \quad . \tag{5}$$

□

The left–hand side of Eq. (5) is referred to as representing the conjugation of rotations.

Geometrical objects of $\mathbb{S}^3 \subset \mathbb{H}$ and of $\mathbb{S}^2 \subset \mathbb{R}^3$

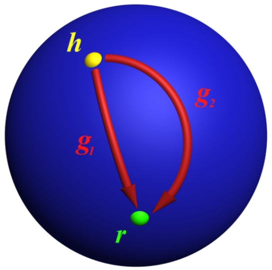

What is the geometrical characterization of the set of all rotations mapping $\mathbf{h} \in \mathbb{S}^2 \subset \mathbb{R}^3$ on $\mathbf{r} \in \mathbb{S}^2$.

Circle of quaternions (1)

Definition

Let $q_1, q_2 \in \mathbb{S}^3$ be two orthogonal unit quaternions. The set of quaternions

$$q(t) = q_1 \cos t + q_2 \sin t, \quad t \in [0, 2\pi),$$

parametrizes the great–circle denoted $C(q_1, q_2) \subset \mathbb{S}^3$.

Proposition

$$q(t) q_1^* q_2 q^*(t) = q_2 q_1^*, \quad t \in [0, 2\pi)$$

where $q_1^* q_2, q_2 q_1^*$ are pure quaternions as q_1 and q_2 are orthogonal.

Circle of quaternions (2)

For example

$$q_1 = \frac{1 - rh}{\|1 - rh\|} \text{ and } q_2 = \frac{h + r}{\|h + r\|} \tag{6}$$

for $\mathbf{h}, \mathbf{r} \in \mathbb{S}^2$ with $\mathbf{r} \neq -\mathbf{h}$.

Obviously, $(\mathbf{h}, \mathbf{r})$ and $(-\mathbf{h}, -\mathbf{r})$ define the same great circle $C(q_1, q_2) \subset \mathbb{S}^3$.

Torus of quaternions

Definition

Let $q_1, q_2, q_3, q_4 \in \mathbb{S}^3$ be four mutually orthonormal quaternions; let $C(q_1, q_2)$ denote the circle spanned by quaternions q_1, q_2, and $C(q_3, q_4)$ the orthogonal circle spanned by q_3, q_4. The set of quaternions

$$q(s, t; \Theta) = \Big(q_1 \cos s + q_2 \sin s\Big) \cos \Theta + \Big(q_3 \cos t + q_4 \sin t\Big) \sin \Theta, \tag{7}$$
$$s, t \in [0, 2\pi), \quad \Theta \in [0, \pi/2]$$

parametrizes the spherical torus denoted $T(C(q_1, q_2); \Theta) \subset \mathbb{S}^3$ with core $C(q_1, q_2)$.

It is actually known as **Clifford torus**, too.

Small circle of unit vectors (1)

Definition

Let $\mathbf{r} \in \mathbb{S}^2$ be a unit vector and

$$r(t) = \cos\frac{t}{2} + \mathbf{r}\sin\frac{t}{2}, \quad t \in [0, 2\pi),$$

represent the rotation about $\mathbf{r}$ by $t \in [0, 2\pi)$. Then the set of unit vectors

$$\mathbf{r}'(t) = r(t)\,\mathbf{r}'_0\,r^*(t), \quad t \in [0, 2\pi), \tag{8}$$

with $\mathbf{r}'_0 \in \mathbb{S}^2$ in the plane spanned by $\mathbf{h}$ and $\mathbf{r}$ such that $\mathbf{r} \cdot \mathbf{r}'_0 = \cos(\rho), \mathbf{h} \cdot \mathbf{r}'_0 = \cos(\eta - \rho)$ parametrizes the small circle or cone

$$c(\mathbf{r}; \rho) = \{\mathbf{r}' \in \mathbb{S}^2 \,|\, \mathbf{r} \cdot \mathbf{r}' = \cos\rho\} \subset \mathbb{S}^2$$

with angle ρ with respect to its centre $\mathbf{r}$.

Small circle of unit vectors (2)

Its parametrized form explicitly reads (e.g. Altmann, 1986)

$$\mathbf{r}'(t) = \mathbf{r}'_0 \cos t + (\mathbf{r} \times \mathbf{r}'_0) \sin t + (\mathbf{r} \cdot \mathbf{r}'_0)\,\mathbf{r}\,(1 - \cos t), \quad t \in [0, 2\pi).$$

Analogously for $\mathbf{h} \in \mathbb{S}^2$,

$$h(t) = \cos\frac{t}{2} + \mathbf{h}\sin\frac{t}{2}, \quad t \in [0, 2\pi),$$

representing the rotation about $\mathbf{h}$ by $t \in [0, 2\pi)$ and $\mathbf{h}'_0 \in \mathbb{S}^2$ in the plane spanned by $\mathbf{h}$ and $\mathbf{r}$ such that
$\mathbf{h} \cdot \mathbf{h}'_0 = \cos(\rho), \mathbf{r} \cdot \mathbf{h}'_0 = \cos(\eta + \rho)$ results in

$$\mathbf{h}'(t) = h(t)\,\mathbf{h}'_0\,h^*(t), \quad t \in [0, 2\pi). \tag{9}$$

Point–to–point rotation by circle of quaternions (1)

Proposition

The fibre $G(\mathbf{h}, \mathbf{r})$ of all rotations with $\mathbf{g}\,\mathbf{h} = \mathbf{r}$ is represented by the circle $C(q_1, q_2) \subset \mathbb{S}^3$ spanned by unit quaternions $q_1, q_2 \in \mathbb{S}^3$ given in terms of $\mathbf{h}, \mathbf{r} \in \mathbb{S}^2$ by Eqs. (6), for example.

Since $q(t)$ and $-q(t)$ represent the same rotation, the circle $C(q_1, q_2)$ covers the fibre $G(\mathbf{h}, \mathbf{r})$ twice.

Thus the major property of the circle $C(q_1, q_2) \equiv C_{\mathbf{h},\mathbf{r}}$ is that it is uniquely characterized by a pair $(\mathbf{h}, \mathbf{r}) \in \mathbb{S}^2 \times \mathbb{S}^2$ and its antipodally symmetric $(-\mathbf{h}, -\mathbf{r})$ in the way that it consists of all quaternions $q(t), t \in [0, 2\pi)$, with $q(t)\,\mathbf{h}\,q^*(t) = \mathbf{r}$ for all $t \in [0, 2\pi)$, and that it covers the fibre $G(\mathbf{h}, \mathbf{r})$ twice.

Point–to–point rotation by circle of quaternions (2)

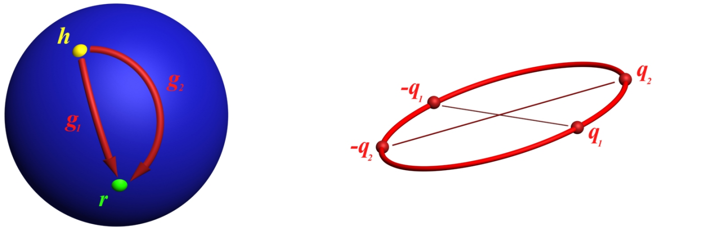

The fibre $G(\mathbf{h}, \mathbf{r})$ of all rotations mapping $\mathbf{h} \in \mathbb{S}^2 \subset \mathbb{R}^3$ on $\mathbf{r} \in \mathbb{S}^2$ is represented by a great circle $C_{\mathbf{h},\mathbf{r}} \subset \mathbb{S}^3 \subset \mathbb{H}$.

Point–to–point rotation by circle of quaternions (3)

Proposition

The two circles $C(q_1, q_2)$ and $C(q_3, q_4)$ representing the fibres $G(\mathbf{h}, \mathbf{r})$ and $G(-\mathbf{h}, \mathbf{r})$, respectively, are orthonormal to one another.

Double fibration

Obviously, $G(\mathbf{h}, \mathbf{r})$, $\mathbf{h}, \mathbf{r} \in \mathbb{S}^2$, induces a double fibration or double covering of $\mathbf{SO}(3)$ as

$$\bigcup_{\mathbf{h} \in \mathbb{S}^2} G(\mathbf{h}, \mathbf{r}) = \bigcup_{\mathbf{r} \in \mathbb{S}^2} G(\mathbf{h}, \mathbf{r}) = \mathbf{SO}(3)$$

for any fixed $\mathbf{r}$ or fixed $\mathbf{h}$, respectively.

In the same way, the 1–dimensional geodesics, i.e. the great circles $C_{\mathbf{h},\mathbf{r}} \subset \mathbb{S}^3$, induce a double fibration of $\mathbb{S}^3$.

In fact, they are actually **Hopf fibres**.

Point–to–point rotation by circle of quaternions (3)

Since

$$q(t)\mathbf{h}q^*(t) = \mathbf{r} \text{ implies that } q(t)\mathbf{h}'q^*(t) \cdot \mathbf{r} = \mathbf{h}' \cdot q^*(t)\mathbf{r}q(t) = \mathbf{h}'\mathbf{h}$$

for all $q(t) \in C(q_1, q_2)$, the set $\{q(t)\mathbf{h}'q^*(t)\}$ represents the small circle (cone) around $\mathbf{r}$ with angle $\arccos \mathbf{h}\mathbf{h}'$.

Point–to–small circle rotation and vv by torus of quaternions (1)

Proposition

The set of all rotations mapping $\mathbf{h}$ on the small circle $c(\mathbf{r}; \rho)$ is equal to the set of all rotations mapping all elements of the small circle $c(\mathbf{h}; \rho)$ onto $\mathbf{r}$ and represented by the spherical torus $T(C(q_1, q_2); \frac{\rho}{2}) \subset \mathbb{S}^3$ with core $C(q_1, q_2)$.

The torus provides a multiple representation of the two sets of rotations.

Point–to–small circle rotation and vv by torus of quaternions (2)

The set of all rotations mapping $\mathbf{h} \in \mathbb{S}^2$ on the small circle $c(\mathbf{r};\rho) \subset \mathbb{S}^2$ is equal to the set of all rotations mapping the small circle $c(\mathbf{h};\rho)$ on $\mathbf{r}$, and it is represented by the torus $T(C;\rho/2) \subset \mathbb{S}^3$.

Point–to–small circle rotation and vv by torus of quaternions (3)

Let $(\mathbf{h},\mathbf{u}),(\mathbf{r},\mathbf{v}) \in \mathbb{S}^2 \times \mathbb{S}^2$ with $\mathbf{u}\cdot\mathbf{v} = \cos\rho$. Then $C_1 \equiv C_{\mathbf{h},\mathbf{u}} \subset \mathbb{S}^3$ and $C_2 \equiv C_{\mathbf{r},\mathbf{v}} \subset \mathbb{S}^3$ exist such that

$$\begin{aligned} p_1 \mathbf{h} p_1^* &= \mathbf{u} \text{ for all } p_1 \in C_1 \\ p_2 \mathbf{r} p_2^* &= \mathbf{v} \text{ for all } p_2 \in C_2 \end{aligned}$$

Then $p_2^* p_1$ maps $\mathbf{h}$ on the small circle with centre $\mathbf{r}$ and angle $\rho = \arccos(\mathbf{u}\cdot\mathbf{v})$ as

$$p_2^* p_1 \mathbf{h} p_1^* p_2 \cdot \mathbf{r} = p_1 \mathbf{h} p_1^* \cdot p_2 \mathbf{r} p_2^* = \mathbf{u}\cdot\mathbf{v}, \qquad (10)$$

Proposition

The representation of the torus $T(C_{\mathbf{h},\mathbf{r}};\frac{\rho}{2})$ can be factorized in terms of $C_{\mathbf{h},\mathbf{u}}$ and $C_{\mathbf{r},\mathbf{v}}$ as

$$T(C_{\mathbf{h},\mathbf{r}};\rho/2) = \{p_2^* p_1 \,|\, p_1 \in C_{\mathbf{h},\mathbf{u}},\ p_2 \in C_{\mathbf{r},\mathbf{v}},\ \mathbf{u}\cdot\mathbf{v} = \cos\rho\} \qquad (11)$$

Point–to–small circle rotation and vv by torus of quaternions (4)

Proposition

The distance d of an arbitrary $q \in \mathbb{S}^3$ from the circle $C(q_1,q_2)$ is given by

$$d(q, C(q_1,q_2)) = \frac{1}{2}\arccos(q\mathbf{h}q^* \cdot \mathbf{r})$$

If $d(q, C(q_1,q_2)) = \rho$, then q and C are called ρ-incident.

Then, the torus $T(C(q_1,q_2);\frac{\rho}{2})$ consisting of all *quaternions* with distance $\frac{\rho}{2}$ from $C(q_1,q_2)$ essentially consists of all *circles* with distance $\frac{\rho}{2}$ from $C(q_1,q_2)$ representing all rotations mapping $\mathbf{h}$ on $c(\mathbf{r};\rho)$ and mapping $c(\mathbf{h};\rho)$ on $\mathbf{r}$.

Point–to–small circle rotation and vv by torus of quaternions (5)

Taking a second look at the equation

$$d(q, C(q_1,q_2)) = d(q, C_{\mathbf{h},\mathbf{r}}) = \frac{1}{2}\arccos(q\mathbf{h}q^*\cdot\mathbf{r}) = \frac{\rho}{2} \ ,$$

we may ask ourselves: Keeping q fixed, for which pairs $(\mathbf{h},\mathbf{r}) \in \mathbb{S}^2 \times \mathbb{S}^2$ is the equation above satisfied?

Obviously, the answer is:

It is satisfied for any $\mathbf{h} \in \mathbb{S}^2$, if $\mathbf{r} \in c(q\mathbf{h}q^*;\rho)$.

Equivalently, it is satisfied for any $\mathbf{r} \in \mathbb{S}^2$, if $\mathbf{h} \in c(q^*\mathbf{r}q;\rho)$.

Geometry of rotations

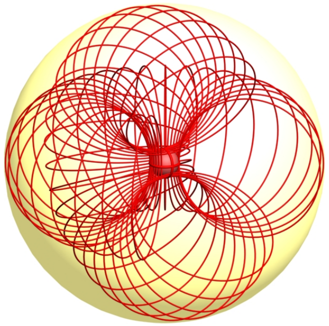

The set of all circles $C(p_1, p_2) \subset \mathbb{S}^3$ tangential to the sphere $s(q; \rho/2)$ with centre q and radius $\rho/2$.

Geometry of rotations

Eventually,

Proposition

The set of all circles $C(p_1, p_2) \subset \mathbb{S}^3$ with a fixed distance $\frac{\rho}{2}$ of a given $q \in \mathbb{S}^3$, i.e. the set of all circles tangential to the sphere $s(q; \rho/2)$ with centre q and radius $\rho/2$, is characterized by

$$\frac{\rho}{2} = d\Big(q, C(p_1, p_2)\Big) = \frac{1}{2} \arccos\Big(q\, \mathbf{h}\, q^* \cdot \mathbf{r}\Big), \tag{12}$$

where $\mathbf{r} \in \mathbb{S}^2$ is uniquely defined in terms of $\mathbf{h}$ and p_1, p_2 by $\mathbf{r} := p(t)\, \mathbf{h}\, p^*(t)$ for all $p(t) \in C(p_1, p_2)$ and any arbitrary $\mathbf{h} \in \mathbb{S}^2$, i.e. each circle $C(p_1, p_2)$ represents all rotations mapping some $\mathbf{h} \in \mathbb{S}^2$ onto an element of the small circle $c(q\mathbf{h}q^*; \rho)$.

Geometry of rotations

Thus, for any $q \in \mathbb{S}^3$ and $\rho \in [0, \pi)$

$$\begin{aligned}\Big\{C(p_1, p_2) \,|\, d\Big(q, C(p_1, p_2)\Big) = \frac{\rho}{2}\Big\} &= \bigcup_{\mathbf{h} \in \mathbb{S}^2} \quad \bigcup_{\mathbf{r} \in c(q\, \mathbf{h}\, q^*; \rho)} C_{\mathbf{h},\mathbf{r}} \qquad (13)\\ &= \bigcup_{\mathbf{h} \in \mathbb{S}^2} \quad \bigcup_{\mathbf{r} \in c(q\, \mathbf{h}\, q^*; \rho)} C(p_1(\mathbf{h}, \mathbf{r}), p_2(\mathbf{h}, \mathbf{r}))\\ &= \bigcup_{\mathbf{h} \in \mathbb{S}^2_+} \quad \bigcup_{\mathbf{r} \in c(q\, \mathbf{h}\, q^*; \rho)} C(p_1(\mathbf{h}, \mathbf{r}), p_2(\mathbf{h}, \mathbf{r})),\end{aligned}$$

where $\mathbb{S}^2_+$ denotes the upper hemisphere of $\mathbb{S}^2$. The last equation is due to the fact that $(\mathbf{h}, \mathbf{r})$ and $(-\mathbf{h}, -\mathbf{r})$ characterize the same great circle $C_{\mathbf{h},\mathbf{r}} \equiv C_{-\mathbf{h},-\mathbf{r}}$.

Geometry of rotations

Proposition

The distance of $q(t) \in C(q_1, q_2)$ from an arbitrary circle C_1 representing all rotations mapping $\mathbf{h}_1$ on $\mathbf{r}_1$ is given by spherical trigonometry

$$\begin{aligned} d(q(t), C_1) &= \frac{1}{2} \arccos\Big(q(t)\mathbf{h}_1 q^*(t) \cdot \mathbf{r}_1\Big) = \frac{1}{2} \arccos\Big(\mathbf{r}' \cdot \mathbf{r}_1\Big)\\ &= \frac{1}{2} \arccos\Big((\mathbf{h} \cdot \mathbf{h}_1)\,(\mathbf{r} \cdot \mathbf{r}_1) + \sqrt{1 - (\mathbf{h} \cdot \mathbf{h}_1)^2}\sqrt{1 - (\mathbf{r} \cdot \mathbf{r}_1)^2}\, \cos t\Big)\\ &= \frac{1}{2} \arccos\Big(\cos\rho\, \cos\eta + \sin\rho\, \sin\eta\, \cos t\Big)\,. \end{aligned} \tag{14}$$

Geometry of rotations

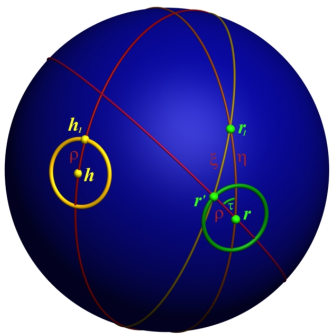

$$d(q(t), C_1) = \xi = \frac{1}{2} \arccos\Big(\cos\rho\, \cos\eta + \sin\rho\, \sin\eta\, \cos t\Big) .$$

The end

$\gg$ **Alles Gerade ist vom Teufel** $\ll$
Kant?, Leibniz?

$\gg$ **Alles Leben ist in Kreisen** $\ll$
Indianisches Sprichwort

Part III

Spherical Integral Transforms

Totally geodesic Radon transform

Let $\mathcal{C}$ denote the set of all 1–dimensional totally geodesic submanifolds $C \subset \mathbb{S}^3$. Each $C \in \mathcal{C}$ is a 1–sphere, i.e. a circle with centre $\mathcal{O}$. Each circle is characterized by a unique pair of unit vectors $\mathbf{h}, \mathbf{r} \in \mathbb{S}^2 \times \mathbb{S}^2$ by virtue of $q\,\mathbf{h}\,q^* = \mathbf{r}$ for all $q \in C$.

Definition

The 1–dimensional totally geodesic Radon transform of a real $f : \mathbb{S}^3 \mapsto \mathbb{R}^1$ is defined as

$$\frac{1}{2\pi} \int_C f(q)\, d\omega_1(q) = (\mathcal{R}_1 f)(C) \equiv \mathcal{R}f(\mathbf{h}, \mathbf{r}).$$

It associates with the function f its mean values over circles $C \in \mathcal{C}$. Then

$$P(\mathbf{h}, \mathbf{r}) = \frac{1}{2}\Big((\mathcal{R}_1 f)(C_{\mathbf{h},\mathbf{r}}) + (\mathcal{R}_1 f)(C_{-\mathbf{h},\mathbf{r}})\Big) = (\mathcal{X}f)(\mathbf{h}, \mathbf{r}), \quad (15)$$

where $\mathcal{X}f$ is referred to as basic *crystallographic* X–ray transform.

Properties of the totally geodesic Radon transform

As a function of $\boldsymbol{g} \mapsto (\mathcal{R}_1 f)(\mathbf{h}, \boldsymbol{g}\,\mathbf{h})$, the 1d Radon transform

$$(\mathcal{R}_1 f)(\mathbf{h}, \mathbf{r}) = \frac{1}{2\pi} \int_{G(\mathbf{h},\mathbf{r})} f(\boldsymbol{g}) d\boldsymbol{g}$$

is constant on the fibres $G(\mathbf{h}, \mathbf{r})$, i.e. for all $\boldsymbol{g} \in G(\mathbf{h}, \mathbf{r})$.

The 1d Radon transform $(\mathcal{R}_1 f)(\mathbf{h}, \mathbf{r})$ satisfies the Darboux–type differential equation

$$(\Delta_{\mathbf{h}} - \Delta_{\mathbf{r}}) \, (\mathcal{R}_1 f)(\mathbf{h}, \mathbf{r}) = 0$$

where $\Delta_{\mathbf{h}}$ stands for the spherical Laplacian with respect to the spherical coordinates of $\mathbf{h}$.

Generalized totally geodesic Radon transform

Definition
The generalized 1–dimensional totally geodesic Radon transform of a real function $f : \mathbb{S}^3 \mapsto \mathbb{R}^1$ is defined as

$$(\mathcal{R}_1^{(\rho)} f)(C) = \frac{1}{4\pi^2 \sin\rho} \int_{d(q,C)=\rho} f(q)\, dq.$$

It associates with f its mean values over the torus $T(C, \rho)$ with core $C \equiv C_{\mathbf{h},\mathbf{r}}$ and radius ρ.

Spherically generalized translation

Definition
The spherically generalized translation of a function $F : \mathbb{S}^2 \mapsto \mathbb{R}^1$ is defined

$$(\mathcal{T}_\rho F)(\mathbf{r}) = \frac{1}{2\pi\sqrt{1-\cos^2\rho}} \int_{\mathbf{r}\mathbf{r}'=\cos\rho} F(\mathbf{r}') d\omega_2(\mathbf{r}').$$

It can be determined by

$$(\mathcal{T}_\rho F)(\mathbf{r}) = \frac{1}{2\pi\sqrt{1-\cos^2\rho}} \int_0^{2\pi} F(\mathbf{r}'(t)) dt,$$

with $\mathbf{r}'(t)$ given according to

$$\mathbf{r}'(t) = r(t)\,\mathbf{r}'_0\, r^*(t), \quad t \in [0, 2\pi),$$

with $\mathbf{r}'_0 \in \mathbb{S}^2$ in the plane spanned by $\mathbf{h}$ and $\mathbf{r}$ such that $\mathbf{r} \cdot \mathbf{r}'_0 = \cos(\rho), \mathbf{h} \cdot \mathbf{r}'_0 = \cos(\eta - \rho)$.

Spherically generalized translation of a Radon transfom

When the translation $\mathcal{T}_\rho$ is applied to the Radon transform with respect to one of its arguments, then the geometry of rotations represented by quaternions amounts to

$$\begin{aligned}
\Big(\mathcal{T}_\rho[\mathcal{R}_1 f]\Big)(\mathbf{h}, \mathbf{r}) &= \frac{1}{2\pi \sin\rho} \int_{c(\mathbf{h};\rho)} (\mathcal{R}_1 f)(\mathbf{h}', \mathbf{r}) d\mathbf{h}' \\
&= \frac{1}{2\pi \sin\rho} \int_{c(\mathbf{r};\rho)} (\mathcal{R}_1 f)(\mathbf{h}, \mathbf{r}') d\mathbf{r}' && (16) \\
&= \frac{1}{4\pi^2 \sin\rho} \int_{T(C(q_1(\mathbf{h},\mathbf{r}), q_2(\mathbf{h},\mathbf{r})); \frac{\rho}{2})} f(q) dq && (17) \\
&= (\mathcal{R}_1^{(\rho/2)} f)(C_{\mathbf{h},\mathbf{r}}). && (18)
\end{aligned}$$

Eq. 16, cf. (Bunge, 1969, p. 47; Bunge, 1982, p. 76), is an Ásgeirsson–type mean value theorem (cf. Ásgeirsson, 1937; John, 1938) justifying the application of $\mathcal{T}_\rho$ to $\mathcal{R}_1 f$ regardless of the order of its arguments, and Eq. 17 is instrumental to the inversion of the totally geodesic Radon transform (Helgason, 1994; 1999).

Inverse Radon transform (1)

In texture analysis, i.e. in material science and engineering, the best known inversion formula dates back right to the beginning of "quantitative" texture analysis. The formula may be rewritten in a rather abstract "Fourier slice" way as

$$f = \mathcal{F}^{-1}_{SO(3)}\, \mathcal{S}\, \mathcal{F}_{\mathbb{S}^2 \times \mathbb{S}^2}\, \mathcal{R} f \ ,$$

where $\mathcal{S}$ denotes a scaling matrix with entries $\sqrt{2\ell+1}$ indicating the ill–posedness of the inverse problem.

Inverse Radon transform (2)

In terms of $(\mathbf{h}, \mathbf{r}) \in \mathbb{S}^2 \times \mathbb{S}^2$ parameterizing the 1–dimensional fibre $G(\mathbf{h}, \mathbf{r})$, the dual Radon transform of any real function P defined on $\mathbb{S}^2 \times \mathbb{S}^2$ is given by

$$\begin{aligned}(\mathcal{R}^*[P(\circ,\circ)])(\boldsymbol{g}) &= \frac{1}{2\pi}\int_{\{(\mathbf{h},\mathbf{r})\in\mathbb{S}^2\times\mathbb{S}^2 \,|\, \boldsymbol{g}\mathbf{h}=\mathbf{r}\}} P(\mathbf{h},\mathbf{r})d(\mathbf{h},\mathbf{r}) \\ &= \frac{1}{2\pi}\int_{\mathbb{S}^2} P(\mathbf{h},\boldsymbol{g}\mathbf{h})d\mathbf{h}\,.\end{aligned}$$

The dual Radon transform is the L^2–adjoint operator of the direct Radon transform, in particular

$$\begin{aligned} f(\boldsymbol{g}) &= \frac{1}{8\pi}\int_{\mathbb{S}^2} (-2\Delta_{\mathbb{S}^2\times\mathbb{S}^2}+1)^{1/2}\mathcal{R}f(\mathbf{h},\boldsymbol{g}\mathbf{h})\,d\mathbf{h} \\ &= \frac{1}{4}\mathcal{R}^*\left[(-2\Delta_{\mathbb{S}^2\times\mathbb{S}^2}+1)^{1/2}\,\mathcal{R}f\right](\boldsymbol{g})\,.\end{aligned}$$

Geometry of rotations

- One of the most beautiful features of quaternions is the role they play in the representation of the rotations of the low dimensional spaces $\mathbb{R}^3$ and $\mathbb{R}^4$.
- Representing rotations by quaternions yields an instructive and geometrically appealing clarification of the geometry of rotations.

The MTEX Project

Crystallographic Orientation

Crystallographic orientation (1)

Neglecting crystal symmetry or assuming triclinic crystal symmetry, the crystallographic orientation $\boldsymbol{g}$ of an individual crystal is the active rotation $\boldsymbol{g} \in G \subset \mathrm{SO}(3)$ which brings a right–handed orthogonal coordinate system $K_{\mathcal{S}}$ fixed to the specimen into coincidence with a right–handed orthogonal coordinate system $K_{\mathcal{C}}$ fixed to the crystal,

$$\boldsymbol{g} \in \mathrm{SO}(3): \; K_{\mathcal{S}} \mapsto K_{\mathcal{C}}.$$

Texture analysis is the analysis of the crystallographic orientation distribution of a polycrystalline specimen.

Orientation imaging is the spatial analysis of the crystallographic orientation distribution of a polycrystalline specimen.

Crystallographic orientation (2)

If the right–handed specimen coordinate system $K_{\mathcal{S}} = < \mathbf{x}, \mathbf{y}, \mathbf{z} >$ and the right–handed crystallographic coordinate system $K_{\mathcal{C}} = < \mathbf{a}, \mathbf{b}, \mathbf{c} >$ are related to one another as

$$\boldsymbol{g}\, K_{\mathcal{S}} = K_{\mathcal{C}}$$

in the sense that

$$\boldsymbol{g}\,\mathbf{x} = \mathbf{a}, \;\; \boldsymbol{g}\,\mathbf{y} = \mathbf{b}, \;\; \boldsymbol{g}\,\mathbf{z} = \mathbf{c}$$

i.e. the crystallographic orientation $\boldsymbol{g}$ brings the specimen coordinate system $K_{\mathcal{S}}$ into coincendence with the crystal coordinate system $K_{\mathcal{C}}$ of an individual crystal, then the vector of coordinates $\mathbf{r}_{K_{\mathcal{S}}} \in \mathbb{S}^2$ with respect $K_{\mathcal{S}}$ of a unique vector and the vector $\mathbf{h}_{K_{\mathcal{C}}} \in \mathbb{S}^2$ of its coordinates with respect to $K_{\mathcal{C}}$ are related to one another by

$$\boldsymbol{g}\,\mathbf{h}_{K_{\mathcal{C}}} = \mathbf{r}_{K_{\mathcal{S}}}$$

Crystallographic Orientation (3)

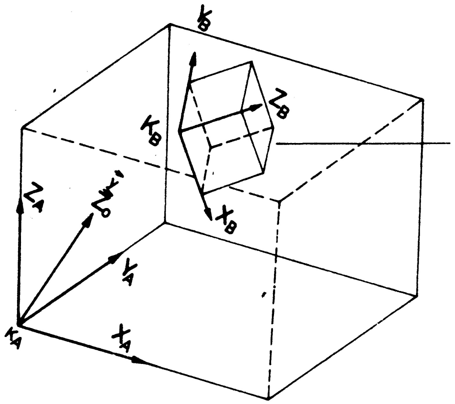

$$\boldsymbol{g} \in G: \; K_{\mathcal{S}} \mapsto K_{\mathcal{C}}$$

(from Matthies, S., 1982, p. 16)

Crystallographic Orientation (4)

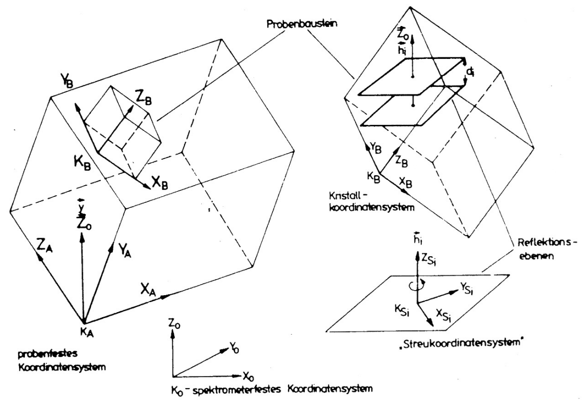

$$\boldsymbol{g}\, K_{\mathcal{S}} = K_{\mathcal{C}}: \;\; \boldsymbol{g}\,\mathbf{h}_{K_{\mathcal{C}}} = \mathbf{r}_{K_{\mathcal{S}}}$$

(from Matthies, S., 1982, p. 16)

Crystallographic Orientation (9)

Let SO(3) denote the special orthogonal group of (proper) rotations, and O(3) the orthogonal group comprising rotations and inversions, thus $\mathrm{O}(3) = \mathrm{SO}(3) \otimes \{id, -id\}$, where $-id$ denotes the symmetry operation of inversion.

Crystallographic Orientation (10)

Let $\mathcal{G}_{\mathcal{C}}$ denote the the crystallographic symmetry class, i.e. a finite point symmetry group; there exist 32 different symmetry classes. They are given by 11 purely rotational groups, 11 Laue groups, and 10 others.

Let

$$G_{\mathcal{C}} := \mathcal{G}_{\mathcal{C}} \cap \mathrm{SO}(3)$$

denote the finite point subgroup of proper rotations associated with the crystal symmetry class $\mathcal{G}_{\mathcal{C}}$, and $\# G_{\mathcal{C}}$ the total number of its elements.

Crystallographic Orientation (12)

Due to Friedel's law the *effective* crystal symmetry is described by the point group

$$\widetilde{\mathcal{G}}_{\mathcal{C}} = \mathcal{G}_{\mathcal{C}} \otimes \{id, -id\}\,,$$

which is also referred to as (associated) Laue class. Out of the 32 symmetry classes the 11 Laue groups contain the operation of inversion as an element of symmetry such that $\mathcal{G}_{\mathcal{C}} = \widetilde{\mathcal{G}}_{\mathcal{C}}$.

Let

$$\widetilde{G}_{\mathcal{C}} := \widetilde{\mathcal{G}}_{\mathcal{C}} \cap \mathrm{SO}(3) = \left(\mathcal{G}_{\mathcal{C}} \otimes \{id, -id\}\right) \cap \mathrm{SO}(3)$$

denote the finite subgroup of proper rotations with respect to the effective crystal symmetry class $\widetilde{\mathcal{G}}_{\mathcal{C}}$.

Crystallographic Orientation (14)

For the 11 purely rotational groups and the 11 Laue groups

$$\widetilde{\mathcal{G}}_{\mathcal{C}} = \mathcal{G}_{\mathcal{C}} \otimes \{id, -id\} = \left(\mathcal{G}_{\mathcal{C}} \cap \mathrm{SO}(3)\right) \otimes \{id, -id\} = G_{\mathcal{C}} \otimes \{id, -id\}$$

holds, implying

$$\widetilde{G}_{\mathcal{C}} = \widetilde{\mathcal{G}}_{\mathcal{C}} \cap \mathrm{SO}(3) = \left(G_{\mathcal{C}} \otimes \{id, -id\}\right) \cap \mathrm{SO}(3) = G_{\mathcal{C}}.$$

Therefore, the total number of their elements is

$$\#\widetilde{\mathcal{G}}_{\mathcal{C}} = 2\,\# G_{\mathcal{C}}\,.$$

For the remaining 10 groups

$$\widetilde{\mathcal{G}}_{\mathcal{C}} \neq G_{\mathcal{C}} \otimes \{id, -id\}, \qquad \widetilde{G}_{\mathcal{C}} \neq G_{\mathcal{C}}$$

In this case, restriction to $G_{\mathcal{C}}$ means an essential loss of information.

Crystallographic Orientation (15)

Example (cf. Matthies and Helming, 1982)

$$\mathcal{G}_{\mathcal{C}} = C_s = \{id, m\}$$

then

$$G_{\mathcal{C}} = \mathcal{G}_{\mathcal{C}} \cap \mathrm{SO}(3) = \{id, m\} \cap \mathrm{SO}(3) = \{id\} = C_1\,,$$

and

$$\widetilde{\mathcal{G}}_{\mathcal{C}} = \mathcal{G}_{\mathcal{C}} \otimes \{id, -id\} = \{id, m\} \otimes \{id, -id\} = \{id, m, -id, C_2\} = C_{2h}\,.$$

However,

$$G_{\mathcal{C}} \otimes \{id, -id\} = \{id, -id\}\,,$$

and is thus different from $\widetilde{\mathcal{G}}_{\mathcal{C}}$.
Also

$$\widetilde{G}_{\mathcal{C}} = \widetilde{\mathcal{G}}_{\mathcal{C}} \cap \mathrm{SO}(3) = \{id, m, -id, C_2\} \cap \mathrm{SO}(3) = \{id, C_2\} \neq G_{\mathcal{C}}\,.$$

Crystallographic Orientation (16)

From group theory it is known that

$$\begin{aligned} \mathrm{O}(3)/\widetilde{\mathcal{G}}_{\mathcal{C}} &= \Big(\mathrm{SO}(3) \otimes \{id, -id\}\Big)/\Big(\mathcal{G}_{\mathcal{C}} \otimes \{id, -id\}\Big) \\ &= \mathrm{SO}(3)/\Big(\widetilde{\mathcal{G}}_{\mathcal{C}} \cap \mathrm{SO}(3)\Big) = \mathrm{SO}(3)/\widetilde{\mathcal{G}}_{\mathcal{C}}. \end{aligned}$$

Eventually, for the 11 purely rotational groups and the 11 Laue groups

$$\mathrm{O}(3)/\widetilde{\mathcal{G}}_{\mathcal{C}} = \mathrm{SO}(3)/G_{\mathcal{C}}.$$

For the remaining 10 groups

$$\mathrm{O}(3)/\widetilde{\mathcal{G}}_{\mathcal{C}} = \mathrm{SO}(3)/\widetilde{G}_{\mathcal{C}} \neq \mathrm{SO}(3)/G_{\mathcal{C}},$$

and the restriction to $\mathrm{SO}(3)/G_{\mathcal{C}}$ means an essential loss of information.

Crystallographic Orientation (17)

When analysing diffraction data for preferred crystallographic orientation it is sufficient to consider the restriction of the Laue group $G_{\mathrm{Laue}} \subset \mathrm{O}(3)$ to its purely rotational part $\widetilde{G}_{\mathrm{Laue}} = G_{\mathrm{Laue}} \cap \mathrm{SO}(3)$.

Then two orientations $g, g' \in \mathrm{SO}(3)$ are called *crystallographically symmetrically equivalent* with respect to $\widetilde{G}_{\mathrm{Laue}}$ if there is a symmetry element $q \in \widetilde{G}_{\mathrm{Laue}}$ such that $gq = g'$.

The left cosets $g\widetilde{G}_{\mathrm{Laue}}$ define the classes of crystallographically symmetrically equivalent orientations.

A function $f : \mathrm{SO}(3) \to \mathbb{R}$ with the property

$$f(g) = f(gq) \text{ for all } q \in \widetilde{G}_{\mathrm{Laue}}$$

is essentially defined on the set of cosets $\mathrm{SO}(3)/\widetilde{G}_{\mathrm{Laue}}$.

Crystallographic Orientation (18)

Analogously, two crystallographic directions $\mathbf{h}, \mathbf{h}' \in \mathbb{S}^2$ are called *crystallographically equivalent* if there is a symmetry element $q \in \widetilde{G}_{\mathrm{Laue}}$ such that $q\mathbf{h} = \mathbf{h}'$.

The MTEX Project

Kernel density estimation with individual orientation measurements (EBSD)

Kernel density estimation

Setting

Let $\boldsymbol{g}_i \in \mathrm{SO}(3), i = 1, \ldots, n$, be individual orientation measurements, and let $\psi_\kappa(\omega(\boldsymbol{g}\boldsymbol{g}_0^{-1}))$ be a kernel, i.e. a non–negative, radially symmetric bell–shaped function on SO(3) well localized around its center $\boldsymbol{g}_0 \in \mathrm{SO}(3)$, with a parameter κ controling its spatial localization.

Kernel density estimator and its Radon transform

Then the kernel density estimator is

$$\widehat{f}_\kappa(\boldsymbol{g};\boldsymbol{g}_1, \ldots, \boldsymbol{g}_n) = \frac{1}{n}\sum_{i=1}^{n} \psi_\kappa(\omega(\boldsymbol{g}\boldsymbol{g}_i^{-1})).$$

and its Radon transform

$$\mathcal{R}[\widehat{f}_\kappa(\circ;\boldsymbol{g}_1, \ldots, \boldsymbol{g}_n)](\mathbf{h}, \mathbf{r}) = \frac{1}{n}\sum_{i=1}^{n} \mathcal{R}\psi_\kappa(\boldsymbol{g}_i\mathbf{h} \cdot \mathbf{r})\,.$$

Kernel density estimation with individual orientation measurements (EBSD)

Kernel density estimator and its Radon transform

Let $g_i \in \mathrm{SO}(3), i = 1, \ldots, n$, be individual orientation measurements, and let $\psi_\kappa(\omega(g\,g_0^{-1}))$ be a kernel, i.e., a non–negative, radially symmetric bell–shaped function on SO(3) well localized around its center $g_0 \in \mathrm{SO}(3)$, with a parameter κ controling its spatial localization.

Then the kernel density estimator is

$$f_\kappa^*(g; g_1, \ldots, g_n) = \frac{1}{n}\sum_{i=1}^{n} \psi_\kappa(\omega(g\,g_i^{-1})).$$

and its Radon transform

$$\mathcal{R}[f_\kappa^*(\circ; g_1, \ldots, g_n)](\mathbf{h}, \mathbf{r}) = \frac{1}{n}\sum_{i=1}^{n} \mathcal{R}\psi_\kappa(g_i\mathbf{h} \cdot \mathbf{r})\,.$$

Estimation of $C_\ell^{kk'}$

Unbiased estimator $\widehat{C}_\ell^{kk'}$

$$\widehat{C}_\ell^{kk'}(\boldsymbol{g}_1, \ldots, \boldsymbol{g}_n) = \frac{1}{n}\sum_{i=1}^{n} T_\ell^{kk'}(\boldsymbol{g}_i), \;\; \ell = 1, \ldots, L$$

Estimation of $C_\ell^{kk'}$

Dirichlet kernel

$$
\begin{aligned}
\psi_L(\omega(\boldsymbol{g}\boldsymbol{g}_0^{-1})) &= \sum_{\ell=0}^{L} \sum_{k,k'=-\ell}^{\ell} (2\ell+1)\, T_L^{kk'}(\boldsymbol{g})\, T_L^{kk'}(\boldsymbol{g}_0) \\
&= \sum_{\ell=0}^{L} (2\ell+1) \frac{\sin\left((2\ell+1)\frac{\omega(\boldsymbol{g}\boldsymbol{g}_0^{-1})}{2}\right)}{\sin\frac{\omega(\boldsymbol{g}\boldsymbol{g}_0^{-1})}{2}} \\
&= \sum_{\ell=0}^{L} (2\ell+1)\, \mathcal{U}_{2\ell}\left(\cos\frac{\omega(\boldsymbol{g}\boldsymbol{g}_0^{-1})}{2}\right)
\end{aligned}
$$

spatial domain | frequency domain

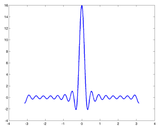

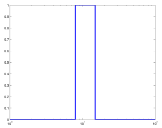

Estimation of $C_\ell^{kk'}$

Harmonic coefficients of Dirichlet kernel density estimator

With the Dirichlet kernel we get

$$
\widehat{f}_{\mathcal{D}_L}(\boldsymbol{g}; \boldsymbol{g}_1, \ldots, \boldsymbol{g}_n) = \frac{1}{n} \sum_{i=1}^{n} \sum_{\ell=0}^{L} (2\ell+1)\, \mathcal{U}_{2\ell}\left(\cos\frac{\omega(\boldsymbol{g}\boldsymbol{g}_i^{-1})}{2}\right)
$$

with

$$
C_\ell^{kk'}(\widehat{f}_{\mathcal{D}_L}) = \begin{cases} \widehat{C}_\ell^{kk'}(\boldsymbol{g}_1, \ldots, \boldsymbol{g}_n), & \text{if } \ell \leq L \\ 0, & \text{otherwise} \end{cases}
$$

which is the

Unbiased estimator $\widehat{C}_\ell^{kk'}$

$$
\widehat{C}_\ell^{kk'}(\boldsymbol{g}_1, \ldots, \boldsymbol{g}_n) = \frac{1}{n} \sum_{i=1}^{n} T_\ell^{kk'}(\boldsymbol{g}_i), \quad \ell = 1, \ldots, L.
$$

The **MTEX** Project

Hematite Texture

Hematite

Hematite, Fe_2O_3, is a trigonal mineral with corundum structure and a hexagonal cell with $a_0 = 0.5038$ nm, $c_0 = 1.3772$ nm.

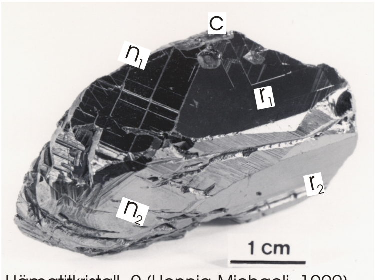

Hämatitkristall 9 (Hennig-Michaeli, 1990)
Minas Gerais, Brasilien, 46 * 23 * 18 mm^3

n {11-23} Bipyramide
r {01-12} Rhomboeder
e {10-14} Rhomboeder

Tetragonal prismatic specimen sized $7 \times 7 \times 14$ mm^3 were prepared from a naturally grown hematite crystal in different crystallographic orientations with their top face either parallel to $c(0001)$, $r(01\bar{1}2)$, $f(10\bar{1}1)$, $a(11\bar{2}0)$, or $m(10\bar{1}0)$, respectively.

Texture analysis based on Neutron diffraction (1)

Neutron diffraction experiment

- Complete pole figures representing the crystallographic preferred orientation of the bulk volume were measured with a neutron texture–diffractometer neutron SV7 at the Research Centre Jülich.
- The reflections of $c(0001)$, $f(10\bar{1}1)$, $r(01\bar{1}2)$, $e(10\bar{1}4)$, and $a(11\bar{2}0)$ were simultaneously measured for a 2Θ-range of 50 degrees using a wavelength of 0.2332 nm, with $c(0001)$ obtained from the third order reflection (0003).
- The standard scanning grid comprising about 500 specimen directions was refined to $14,616$ positions with a mean distance of 1.5 degree. The total measuring time was about three days.

Texture analysis based on Neutron diffraction (2)

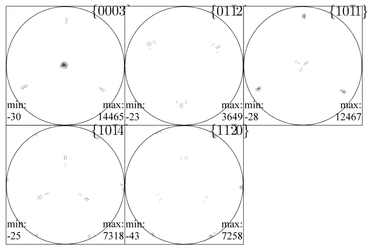

Experimental pole figures (equal area projection, upper hemisphere) of the reflections $c(0001)$, $f(10\bar{1}1)$, $r(01\bar{1}2)$, $e(10\bar{1}4)$, and $a(11\bar{2}0)$ measured by neutron diffraction with specimen H43C1 deformed by 3.4% in compression perpendicular to $c(0001)$.

Texture analysis based on Neutron diffraction (3)

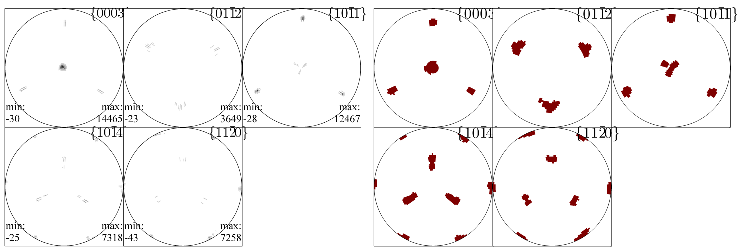

Application of zero–range method which initializes the odf to be zero for all orientations which correspond to a zero–intensity direction in the experimental pole figures depicted in blue.

Then, instead of a total of $743,120$ only a total of 533 de la Vallée Poussin kernels with a halfwidth of 1.5 degree corresponding to a bandwidth of 286 were fitted to explain the data. The time elapsed to compute the ODF was 271 seconds with a notebook equipped with a Core 2 Duo CPU with 1.86 GH cpu–frequency and 2 GB RAM.

Texture analysis based on Neutron diffraction (4)

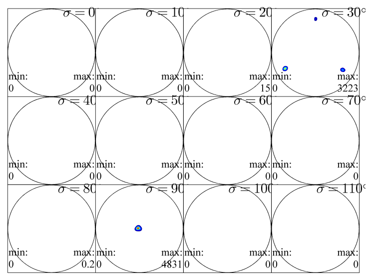

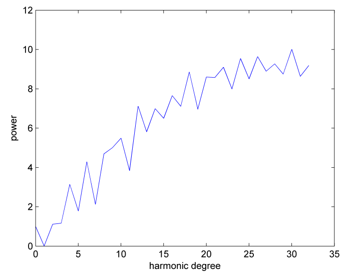

σ–sections and power plot of MTEX's recovered ODF based on experimental pole figures of the reflections $c(0001)$, $r(01\bar{1}2)$, $f(10\bar{1}1)$, $e(10\bar{1}4)$, and $a(11\bar{2}0)$.

Its texture index is approximately $3,400$,
the entropy is approximately -7.35.

Texture analysis based on Neutron diffraction (5)

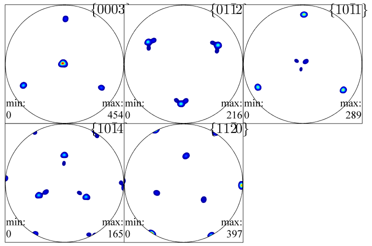

Recalculated pole figures (equal area projection, upper hemisphere) of the reflections $c(0001)$, $r(01\bar{1}2)$, $f(10\bar{1}1)$, $e(10\bar{1}4)$, and $a(11\bar{2}0)$.

The relative ℓ^1–norm errors (RP errors) are
$\mathrm{RP}(0001) = 0.55$, $\mathrm{RP}(01\bar{1}2) = 0.75$, $\mathrm{RP}(10\bar{1}1) = 0.87$,
$\mathrm{RP}(10\bar{1}4) = 0.70$, $\mathrm{RP}(11\bar{2}0) = 0.90$.

Texture analysis based on Neutron diffraction (6)

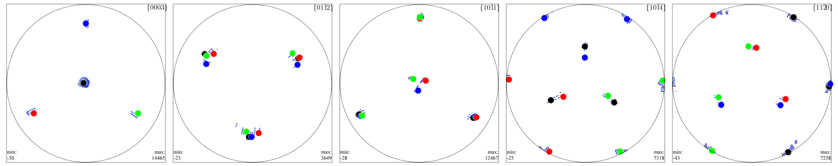

Experimental pole figures (equal area projection, upper hemisphere) of the reflections $c(0001)$, $r(01\bar{1}2)$, $f(10\bar{1}1)$, $e(10\bar{1}4)$, and $a(11\bar{2}0)$ augemented with major mode $(155, 3, 53)$ (black), and minor modes $(90, 65, 59)$ (blue), $(30, 115, 1)$ (red), and $(150, 115, 1)$ (green), respectively.

The major mode depicted black represents the parent crystal orientation, and the three minor modes depicted blue, red, and green, respectively, indicate three r–twin orientations.

Texture analysis based on Neutron diffraction (7)

Neutron	(α, β, γ)	$\int_{b(g_m;10)} f(g)dg$	$f(\alpha, \beta, \gamma)$
g_M (black)	$(155, 3, 53)$	0.45	14, 709
g_{m_1} (blue)	$(90, 65, 59)$	0.09	675
g_{m_2} (red)	$(30, 115, 1)$	0.18	750
g_{m_3} (green)	$(150, 115, 1)$	0.09	545
sum		0.36	

The major mode g_M and the three minor modes $g_{m_i}, i = 1, 2, 3$, are given in terms of Euler angles (α, β, γ) (zyz–convention) (left), and characterized by their probability mass according to the orientation density function in a ball $b(g_m; 10)$ of 10 degrees (center), and their values of the orientation density function $f(g_m)$ (right).

Texture analysis based on EBSDiffraction (1)

Electron back scatter diffraction experiment

- Electron back scatter diffraction (EBSD) measurements were performed on a SEM CamScan CS44LB equipped with an EBSD attachment at ETH Zurich, Switzerland, and a total of 69, 541 individual orientations were measured.
- Using the processing software OIM® (EDAX–TSL Inc.), orientation image microscopy maps (OIM® maps) were acquired.

EBSD data analysis with MTEX

- pole point plots, odf, C–coefficients, texture index, volume portions, orientation maps, etc.

Texture analysis based on EBSDiffraction (2)

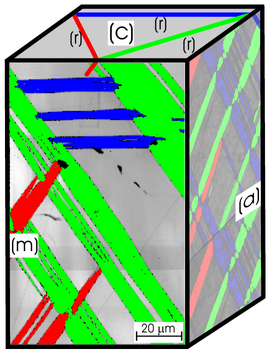

The top face of specimen H43C1 is $c(0001)$, one side face is $a(11\bar{2}0)$, and the other one is $m(10\bar{1}0)$. OIM® maps of both planes are mounted in a 3d–micrograph showing on faces (m) and (a) three sets of r–twin lamellae which are coloured in blue, red, and green.

Texture analysis based on EBSDiffraction (3)

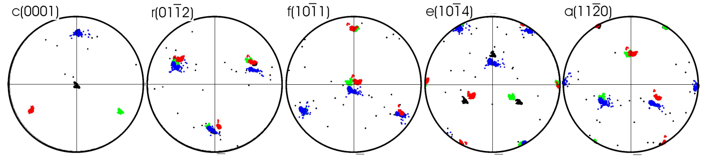

Local pole point OIM® plots (equal area projection, upper hemisphere) of plane $m(10\bar{1}0)$ rotated in a position with the compression direction perpendicular to the plane of projection: parent crystal (black), three r–twins (blue, red, and green). The colours in the pole figures correspond to those in the OIM® maps.

Texture analysis based on EBSDiffraction with MTEX (1)

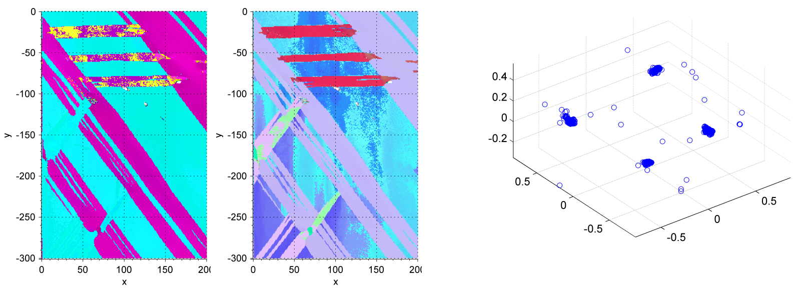

RGB– and IHS–colour coded raw EBSD measurements of specimen H43C1 deformed by 3.4% in compression perpendicular to $c(0001)$ (left and center), EBSD measurements in Rodrigues space (right).

Texture analysis based on EBSDiffraction with MTEX (2)

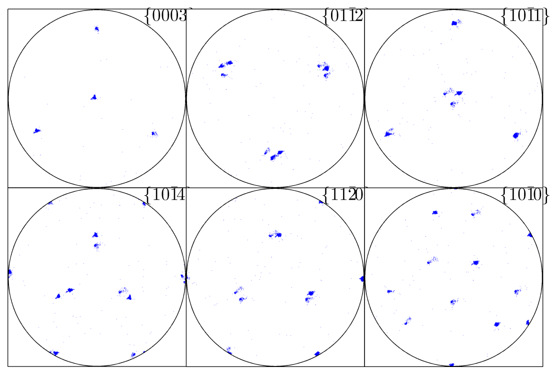

Pole point plots (equal area projection, upper hemisphere) of the crystal forms $c(0001)$,$r(01\bar{1}2)$, $f(10\bar{1}1)$, $e(10\bar{1}4)$, $a(11\bar{2}0)$, and $m(10\bar{1}0)$.

Texture analysis based on EBSDiffraction with MTEX (3)

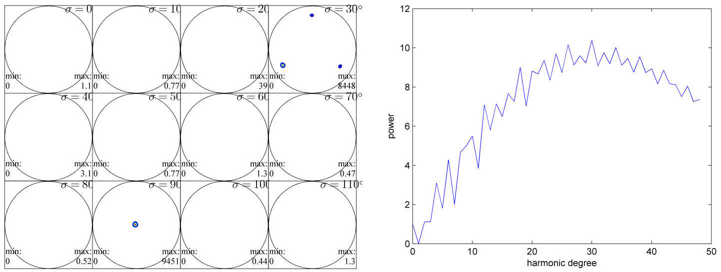

σ–sections and power plot of MTEX's estimated ODF based on EBSD measurements and non–parametric kernel density estimation with the de la Vallée Poussin kernel with a halfwidth of 2.0 degrees corresponding to the finite bandwidth of $L = 213$ of the series expansion into generalized spherical harmonics.

Its texture index is approximately $3,400$,
the entropy is approximately -7.42.

Texture analysis based on EBSDiffraction with MTEX (4)

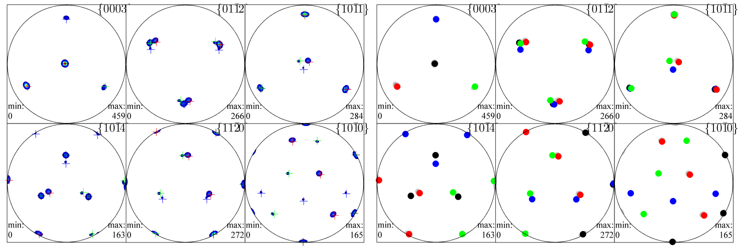

Corresponding computed pole density functions of the crystal forms $c(0001)$, $r(01\bar{1}2)$, $f(10\bar{1}1)$, $e(10\bar{1}4)$, $a(11\bar{2}0)$, and $m(10\bar{1}0)$ augmented with major mode $(100, 178, 11)$ (black), and minor modes $(90, 65, 59)$ (blue), $(30, 115, 1)$ (red), and $(150, 115, 1)$ (green), respectively.

Texture analysis based on EBSDiffraction with MTEX (5)

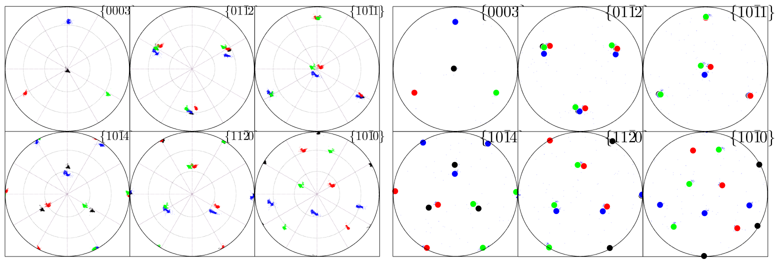

Pole point plots (equal area projection, upper hemisphere) of the crystal forms $c(0001)$, $f(10\bar{1}1)$, $r(01\bar{1}2)$, $e(10\bar{1}4)$, $a(11\bar{2}0)$, and $m(10\bar{1}0)$ colour coded according to their classification according to 10 degree neighbourhoods with respect to modes of the estimated ODF, and augmented with major mode $(100, 178, 11)$ (black), and minor modes $(90, 65, 59)$ (blue), $(30, 115, 1)$ (red), and $(150, 115, 1)$ (green), respectively, computed and displayed with MTEX.

Texture analysis based on EBSDiffraction with MTEX (6)

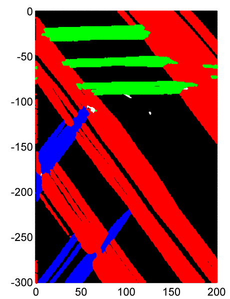

EBSD measurements of specimen H43C1 colour coded according to their classification with respect to modes of the estimated ODF.

Texture analysis based on EBSDiffraction with MTEX (7)

EBSD	(α,β,γ)	$\int_{b(g_m;10)} f(g)dg$	$f(\alpha,\beta,\gamma)$
g_M (black)	$(100,178,11)$	0.45	$12,251$
g_{m_1} (blue)	$(90,65,59)$	0.05	699
g_{m_2} (red)	$(30,115,1)$	0.04	450
g_{m_3} (green)	$(150,115,1)$	0.33	$2,611$
sum		0.42	

The major mode g_M and the three minor modes $g_{m_i}, i = 1,2,3$, are given in terms of Euler angles (α,β,γ) (zyz–convention) (left), and characterized by their probability mass according to the orientation density function in a ball $b(g_m;10)$ of 10 degrees (center), and their values of the orientation density function $f(g_m)$ (right).

Comparison by numbers

Neutron	(α,β,γ)	$\int_{b(g_m;10)} f(g)dg$	$f(\alpha,\beta,\gamma)$
g_M (black)	$(155,3,53)$	0.45	$14,709$
g_{m_1} (blue)	$(90,65,59)$	0.09	675
g_{m_2} (red)	$(30,115,1)$	0.18	750
g_{m_3} (green)	$(150,115,1)$	0.09	545
sum		0.36	

EBSD	(α,β,γ)	$\int_{b(g_m;10)} f(g)dg$	$f(\alpha,\beta,\gamma)$
g_M (black)	$(100,178,11)$	0.45	$12,251$
g_{m_1} (blue)	$(90,65,59)$	0.05	699
g_{m_2} (red)	$(30,115,1)$	0.04	450
g_{m_3} (green)	$(150,115,1)$	0.33	$2,611$
sum		0.42	

Comparison by power plots

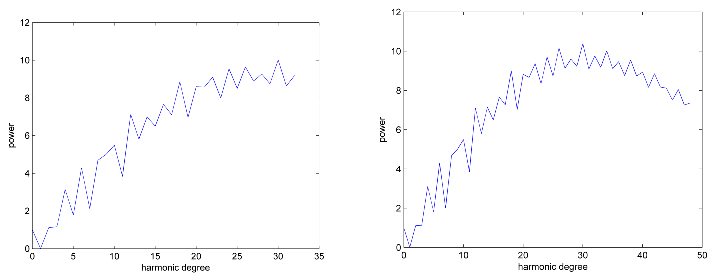

Conclusions

- the results of texture analyses based on integral Neutron diffraction data and on individual electron back scatter diffraction data agree very well;
- an interpretation of an orientation density function in terms of its values may be deceiving. A proper interpretation is accomplished in terms of volume portions only;
- method and software apply to high resolution and sharp textures;
- unique approach to analyse individual or integral orientation measurements facilitates comparison and joint interpretation.

The **MTEX** Project

MTEX Data Model for EBSD Data

Orientation distance

EBSD data are spatially referenced measurements of crystallographic orientations, i.e. $g_i = g(x_i), g \in SO(3)/\widetilde{G}_{\text{Laue}}, x_i \in D \subset \mathbb{R}^d, i = 1, \dots, n$. The difference of any two orientations $g_i, g_j \in SO(3)/\widetilde{G}_{\text{Laue}}$ of the same restricted Laue group $\widetilde{G}_{\text{Laue}}$ is defined as

$$d(g_i, g_j) = \min_{\sigma \in \widetilde{G}_{\text{Laue}}} \omega(g_i \sigma g_j^{-1}). \tag{19}$$

If two different restricted Laue groups are involved, then the orientation difference is defined as

$$d(g_i, g_j) = \min_{\sigma_1 \in \widetilde{G}_{\text{Laue }1}, \sigma_2 \in \widetilde{G}_{\text{Laue }2}} \omega(g_i \sigma_1 \sigma_2 g_j^{-1}). \tag{20}$$

As Eq. (20) is more general, we shall always refer to it even if Eq. (19) applies.

MTEX data model for EBDS data (1)

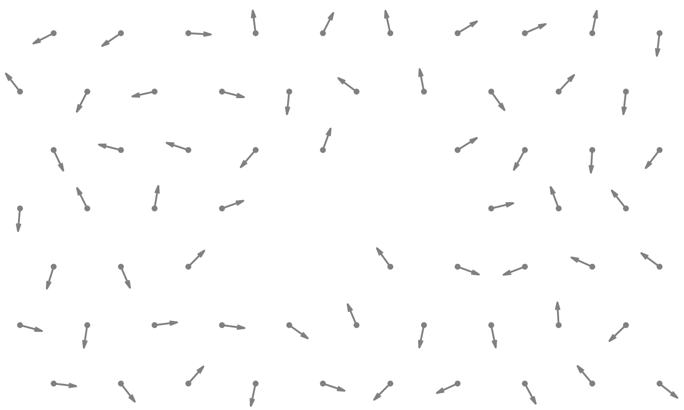

Data $g_i = g(x_i), i = 1, \dots, n$ on an initially regular hexagonal grid with missing data, validated data displayed as arrows are no longer arranged according to a regular grid

MTEX data model for EBDS data (2)

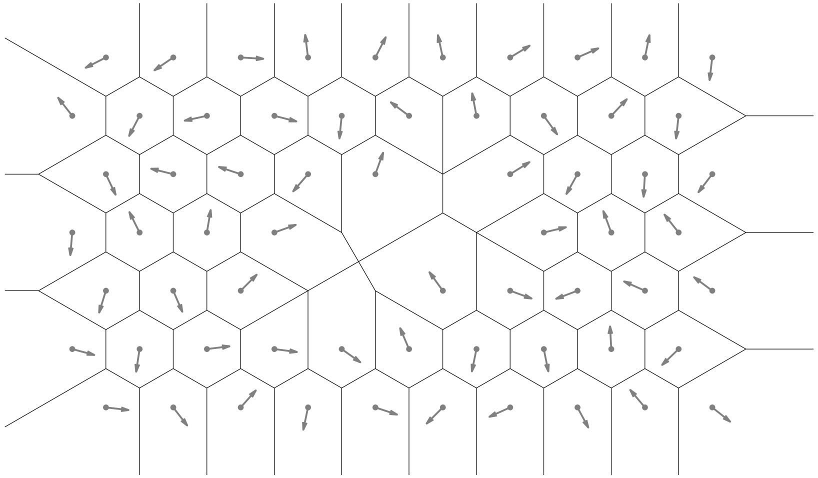

Dirichlet partition into Dirichlet cells $D_i = D(x_i), i = 1, \dots, n$

MTEX data model for EBDS data (3)

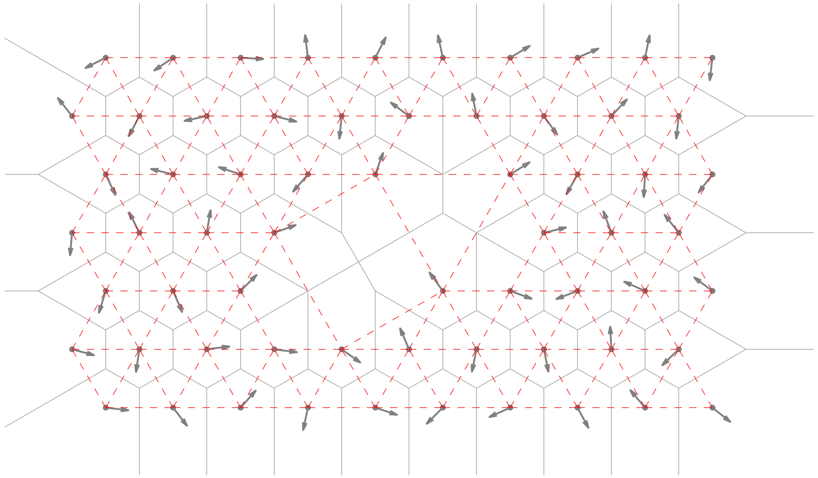

Dirichlet partition and its dual joining adjacent measurement locations by geometrical edges (hatched red lines) generating the Delaunay triangulation of the measurement locations $x_i, i = 1, \ldots, n$, except for ambiguities

MTEX data model for EBDS data (4)

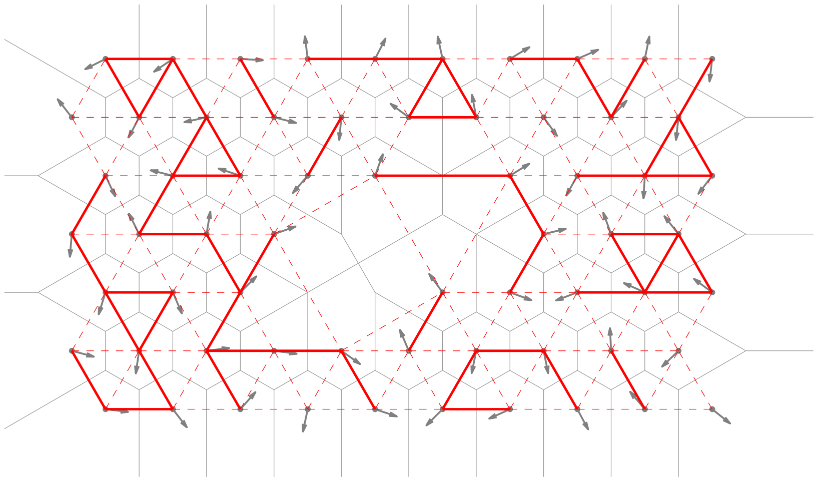

Generating a subgraph (bold red lines) of adjacent measurement locations satisfying the constraint $\measuredangle(\mathbf{g}_i, \mathbf{g}_j) \leq \omega_b$, here with a threshold of $\omega_b = 50°$

MTEX data model for EBDS data (5)

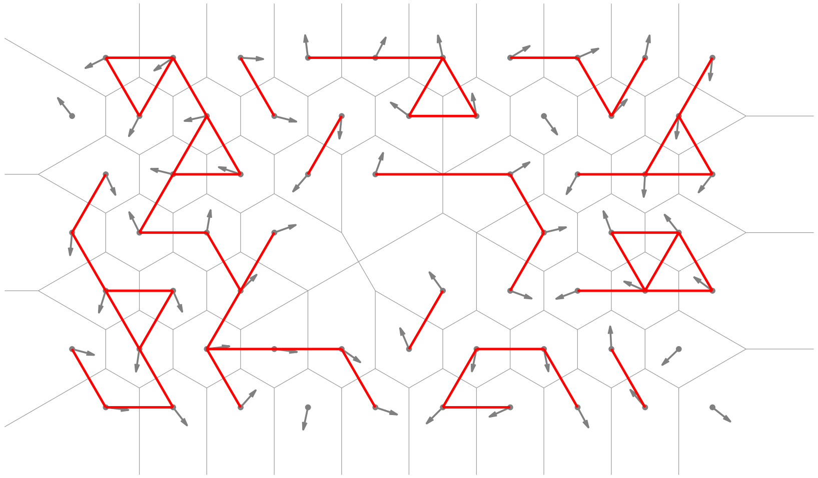

Identifying regions in terms of components of the subgraph, i.e. identifying Dirichlet cells contributing physically to the regions

MTEX data model for EBDS data (6)

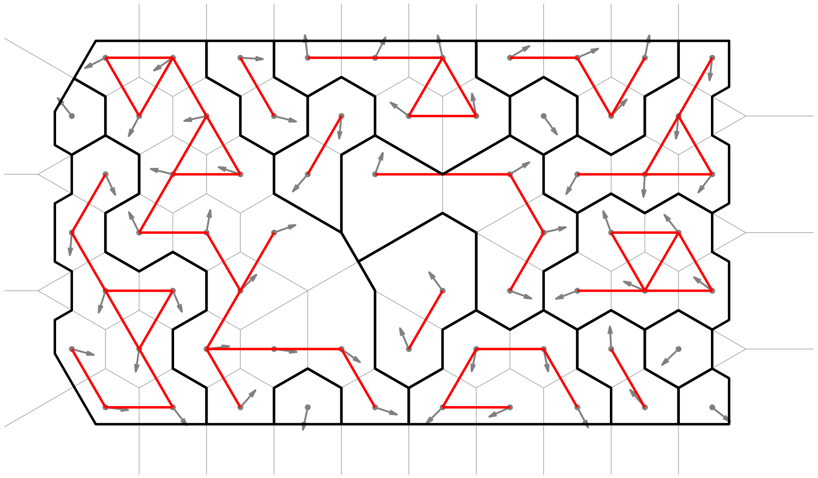

Determining the boundaries (bold black lines) as outlines of the regions

MTEX data model for EBDS data (7)

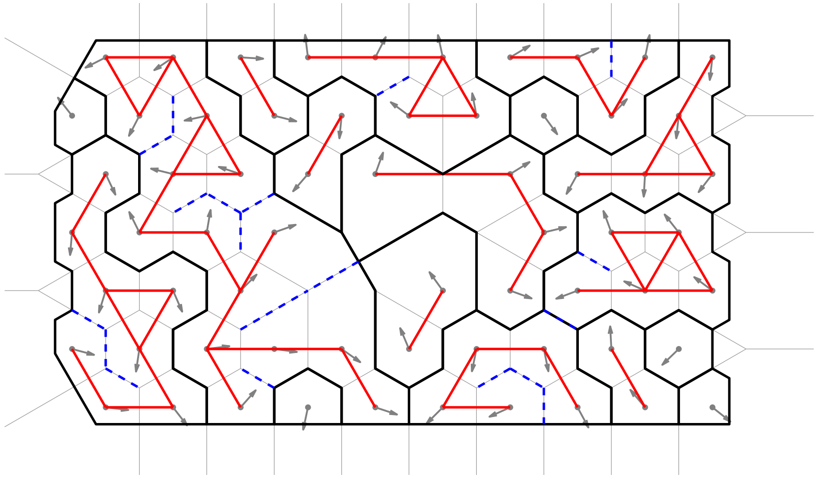

Including interior boundaries (hatched blue lines) separating (initially) adjacent measurement locations within a given region violating the thresholding constraint

MTEX data model for EBDS data (8)

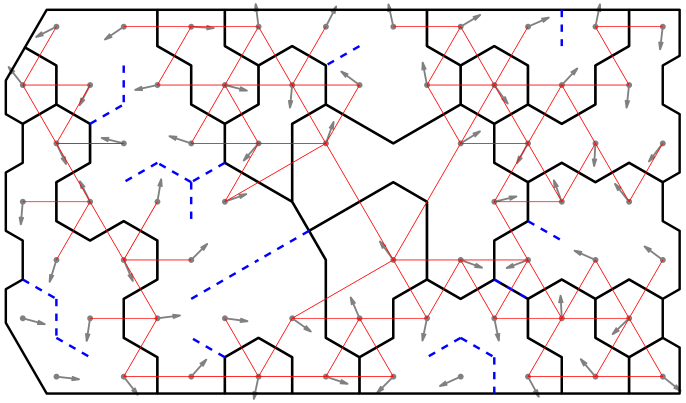

Display of an explicit representation (thin red lines) of the exterior boundary segments (bold black lines) separating (initially) adjacent measurement locations of adjacent regions violating the thresholding constraint

MTEX data model for EBDS data (9)

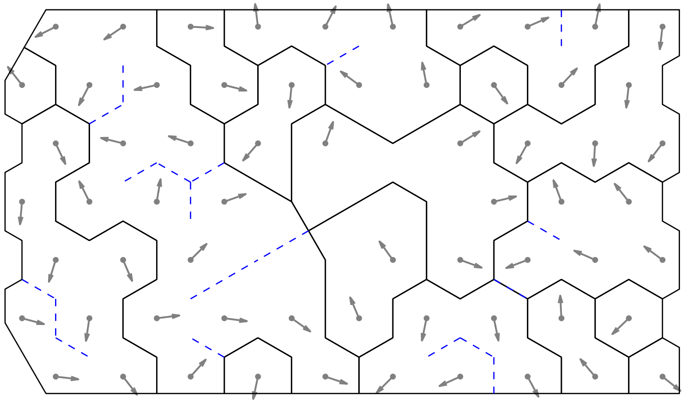

Resulting partition displaying exterior (black lines) and interior (hatched blue lines) grain boundaries

MTEX data model for EBDS data (10)

Let $S = \{x_1, \ldots, x_n\} \subset D \subset \mathbb{R}^d$ be a set of points with $n \geq 2$. Then the half plane for $x_i \neq x_j$

$$H(x_i, x_j) = \{x \in D \mid \| x - x_i \| \leq \| x - x_j \|\} \qquad (21)$$

consists of all points in D which are closer to x_i than to x_j, and the bisector

$$b(x_i, x_j) = \{x \in D \mid \| x - x_i \| = \| x - x_j \|\} \qquad (22)$$

consists of all points equidistant to x_i and x_j. Then

$$D_i = D(x_i) = \bigcap_{j \neq i} H(x_i, x_j) = \{x \in D \mid \| x - x_i \| \leq \| x - x_j \| \text{ for all } j \neq i\} \qquad (23)$$

is the d dimensional Dirichlet cell associated to $x_i \in D$. The set $\mathcal{D}(S) = \{D_i, \ldots, D_n\}$ of all Dirichlet cells associated to the point set S is called Dirichlet partition. The geometrical elements composing the boundary of Dirichlet cells are distinguished in terms of their dimension, i.e. faces, edges, and vertices.

MTEX data model for EBDS data (11)

Two points $x_i, x_j \in D$ and their associated Dirichlet cells are obviously geometrically adjacent if $D(x_i) \cap D(x_j) = b(x_i, x_j) \neq \emptyset$.

Joining adjacent points by edges results in the Delaunay triangulation $\mathcal{T}(S)$. Dirichlet partition and Delaunay triangulation are dual partitions and represented by dual graphs, respectively (Delaunay, 1943; O'Rourke, 1994).

MTEX data model for EBDS data (12)

Enumerating the nodes $\nu_1, \nu_2, \ldots, \nu_n, n \in \mathbb{N}$, and the edges $e_1, \ldots, e_m, m \in \mathbb{N}$, the $(n \times m)$ incidence matrix I_{NE} associated with the graph $\mathcal{G}(N, E)$ is defined as

$$\left(I_{NE}\right)_{ij} = \begin{cases} 1 & \text{if } \nu_i \in e_j \\ 0 & \text{otherwise} \end{cases} \quad i = 1, \ldots, n, \; j = 1, \ldots, m. \tag{24}$$

The $(n \times n)$ adjacency matrix A_N of nodes associated with $\mathcal{G}(N, E)$ is defined as

$$\left(A_N\right)_{ij} = \begin{cases} 1 & \text{if } \{\nu_i, \nu_j\} \in E \\ 0 & \text{otherwise} \end{cases} \quad i, j = 1, \ldots, n. \tag{25}$$

Obviously, the diagonal elements of A_N equal 0.

MTEX data model for EBDS data (13)

Identifying the nodes ν_i of a graph with Dirichlet cells $D(x_i)$ and the edges e_j of the graph with the geometrical edges of the Dirichlet cells, the associated incidence matrix, Eq. (26), and adjacency matrix, Eq. (27), support a geometrical interpretation.

Then $(I_{NE})_{ij} = 1$ indicates that the edge e_j coincides with some bisector $b(x_i, x_k)$ of the Dirichlet cell $D(x_i)$, and $(A_N)_{ij} = 1$ indicates that the two Dirichlet cells $D(x_i), D(x_j)$ share a common bisector $b(x_i, x_j)$.

MTEX data model for EBDS data (12)

Enumerating the nodes $\nu_1, \nu_2, \ldots, \nu_n, n \in \mathbb{N}$, and the edges $e_1, \ldots, e_m, m \in \mathbb{N}$, the $(n \times m)$ incidence matrix I_{NE} associated with the graph $\mathcal{G}(N, E)$ is defined as

$$\left(I_{NE}\right)_{ij} = \begin{cases} 1 & \text{if } \nu_i \in e_j \\ 0 & \text{otherwise} \end{cases} \quad i = 1, \ldots, n, \; j = 1, \ldots, m. \tag{26}$$

The $(n \times n)$ adjacency matrix A_N of nodes associated with $\mathcal{G}(N, E)$ is defined as

$$\left(A_N\right)_{ij} = \begin{cases} 1 & \text{if } \{\nu_i, \nu_j\} \in E \\ 0 & \text{otherwise} \end{cases} \quad i, j = 1, \ldots, n. \tag{27}$$

Obviously, the diagonal elements of A_N equal 0.

MTEX data model for EBDS data (14)

By duality, these matrices bear another geometrical interpretation referring to the corresponding Delaunay triangulation.

If the nodes ν_i are now identified with the points x_i, and the edges e_j with line segments joining x_{j_1} and x_{j_2}, then $(I_{NE})_{ij} = 1$ indicates that the point x_i is an endpoint of the line segment e_j, and $(A_N)_{ij} = 1$ indicates that the two points x_i, x_j are strong Dirichlet neighbours to be joined to an edge of some Delaunay triangle.

MTEX data model for EBDS data (15)

Multiplying the incidence matrix by its transpose,

$$I_{NE}\, I_{NE}^{\mathrm{T}} = \widetilde{A}_N, \tag{28}$$

results in an $(n \times n)$ enhanced adjacency matrix $\widetilde{A}_N$ as its off-diagonal entries coincide with the entries of A_N and its diagonal entries record the total number of adjacent nodes of each node $\nu_i \in N$.

Multiplying A by itself results in the $(n \times n)$ matrix A^2. Its non-zero off-diagonal entries indicate second order adjacency, its diagonal entries record again the total number of adjacent nodes of each node $\nu_i \in N$. More generally, the entries of A^n record the total number of different ways of moving between the corresponding nodes in n steps. Recording the power of A at which an entry first is non-zero results in the matrix whose entries are the topological length of the topologically shortest path (O'Sullivan and Unwin, 2003, 154–161).

Summary of **MTEX** data model for EBDS data

Once grain boundaries and grains are determined with respect to a given threshold ω_b, a wide variety of corresponding variables describing fabric can be derived, e.g.

- summary statistics of the total number of measurements, per phase, per grain, the total number of adjacent grains,
- join–count statistics of phase transitions for adjacent grains,
- distribution of grain size, grain shape, and boundary size,
- directional distribution of grain boundaries,
- orientation distribution analysis per grain,
- various kinds of mis-orientation distributions,
- characteristics of boundaries in terms of phase boundaries, large angle vs. small angle boundaries, twin boundaries,
- etc.,

and their dependence of the threshold ω_b can be analyzed.

The **MTEX** Project

The Bingham quaternion distribution

Introduction

Model orientation distributions support the concept of "Ideallagen" introduced by Grewen and Wassermann, as they are characterized by a rather small number of physically meaningful parameters and they can easily be evaluated numerically with analytical precision.

They allow hypotheses to be tested by methods of spherical statistics, and thus provide explanatory models.

The Bingham quaternion distribution is well suited for this purpose, since its parameter domain allows to simulate a wide range of different texture types. It can be characterized as the first order element of the crystallographic exponential family $\mathbb{CEF}$. Special cases of second order $\mathbb{CEF}$ are shown to represent symmetrcical cone and ring fibre textures.

Parametrization and embedding of rotations

Parametrization

A rotation g may be parametrized by e.g. the corresponding triplet of three Euler angles or by the rotation axis and angle.

Embedding

It may be embedded in $\mathbb{R}^{3\times 3}$ by virtue of a 3×3 matrix $M(g) \in \mathrm{SO}(3)$, the special orthogonal group in $\mathbb{R}^3$, or in $\mathbb{S}^3 \subset \mathbb{H}$ by a virtue of its real unit quaternion $q(g)$. The entries of the matrix $M(g)$ or of the unit quaternion $q(g)$ are given in terms of the parameters of g.

Bingham quaternion distribution on $\mathbb{S}^3$

A random unit quaternion $x \in \mathbb{S}^3$ is said to be distributed according to the Bingham quaternion distribution $B_4(\Lambda, A)$ if it has the probability density function

$$f_{\mathrm{B}}(x;\Lambda,A) \quad = \quad C_B^{-1}(\Lambda)\ \exp\left\{\sum_{i=1}^{4}\lambda_i\left(\mathrm{Sc}(a_i^* x)\right)^2\right\}\ [\,ds_3\,]\ ,$$

where

- ds_3 represents the Lebesgue invariant area element on $\mathbb{S}^3$,
- $A \in SO(4)$ is a (4×4) orthogonal matrix with unit column quaternions $a_i \in \mathbb{S}^3 \subset \mathbb{H}$ such that $\sum_{i=1}^4 \left(\mathrm{Sc}(a_i^* x)\right)^2 = 1$,
- Λ is a (4×4) diagonal matrix with entries $\lambda_1, \dots, \lambda_4$, and
- $C_B(\Lambda)$ is a normalizing constant.

Different sets $\lambda_1, \dots, \lambda_4$ yield bimodal or multimodal distributions with corresponding sets of modes given by the a_i, $i = 1, \dots, 4$.

Von Mises – Fisher matrix distribution on SO(3)

Let $X \in \mathrm{SO}(3)$ be a special orthogonal matrix representing a random rotation in $\mathbb{R}^3$. Then X is said to be distributed according to the von Mises – Fisher matrix distribution $M_3(F)$ if it has the probability density function

$$f_{\mathrm{vMF}}(X;F) = C_{\mathrm{vMF}}^{-1}(F)\exp[\,\mathrm{tr}(FX^t)\,]\,[\,dX\,]\ ,$$

with a (3×3) parameter matrix F and normalizing constant $C_{\mathrm{vMF}}(F)$.

From the polar decomposition $F = KM$ with $K, M \in \mathrm{SO}(3)$, the polar component M is interpreted as the (set of) mode(s) of the distribution, and the elliptical component K as a shape parameter matrix.

Equivalence

$X \in \mathrm{SO}(3)$ has a von Mises – Fisher matrix distribution $M_3(F)$ if and only if $x \in \mathbb{S}^3$ has a Bingham distribution $B_4(\Lambda, A)$ such that for any pair $x(\mathrm{g}) \in \mathbb{S}^3$ and $X(\mathrm{g}) \in \mathrm{SO}(3)$ it holds

$$\mathrm{tr}\,(FX^t) = \sum_{i=1}^{4} \lambda_i \left(\mathrm{Sc}(a_i^* x)\right)^2 \ .$$

Totally geodesic Radon transform

The totally geodesic Radon transform of the Bingham distribution follows from integration along the geodesic $\{x \in \mathbb{S}^3 \,|\, x\,\mathbf{h}\,x^* = \mathbf{r}\}$ as

$$\begin{aligned} (\mathcal{R}f_{\mathrm{B}})(\mathbf{h},\mathbf{r}) &= c_B^{-1}(\Lambda)\,\frac{1}{2\pi}\int_0^{2\pi} \exp\left(\sum_{i=1}^{4}\lambda_i\,\left(\mathrm{Sc}(a_i^* q(t))\right)^2\right) dt \\ &= c_B^{-1}(\Lambda)\,\exp(\xi)\,I_0(\sqrt{\upsilon^2+\zeta^2}) \end{aligned}$$

with

$$\begin{aligned} \xi &= \frac{1}{2}\sum_{i=1}^{4}\lambda_i\left((\mathrm{Sc}(a_i^* q_1))^2 + (\mathrm{Sc}(a_i^* q_2))^2\right), \\ \upsilon &= \frac{1}{2}\sum_{i=1}^{4}\lambda_i\left((\mathrm{Sc}(a_i^* q_1))^2 - (\mathrm{Sc}(a_i^* q_2))^2\right), \\ \zeta &= \sum_{i=1}^{4}\lambda_i\,\mathrm{Sc}(a_i^* q_1)\,\mathrm{Sc}(a_i^* q_2)\,. \end{aligned}$$

Geometrical objects of $\mathbb{S}^3 \subset \mathbb{H}$ (1)

Let $a_i \in \mathbb{S}^3, i = 1, \ldots, 4$, be any set of four orthonormal quaternions. They span

- an axis

$$B(a_4) = \{-a_4, +a_4\}$$

- a unit circle

$$C(a_3, a_4) = \{q(t) \in \mathbb{S}^3 \,|\, q(t) = a_4 \cos t + a_3 \sin t, \ \ t \in [0, 2\pi)\}$$

- a unit sphere

$$\begin{aligned} &S(a_2, a_3, a_4) = \\ &\{q(s,t) \in \mathbb{S}^3 \,|\, q(s,t) = (a_4 \cos t + a_3 \sin t)\sin s + a_2 \cos s, \\ &\ s \in [0, \pi], \ t \in [0, 2\pi)\} \end{aligned}$$

Geometrical objects of $\mathbb{S}^3 \subset \mathbb{H}$ (2)

Obviously, $B(a_1)$ and $S(a_2, a_3, a_4) = a_1^{\perp}$ are mutually orthogonal complements with respect to $\mathbb{S}^3$, and so are $C(a_3, a_4)$ and $C(a_1, a_2)$.

These circles and spheres are centered at $\mathcal{O}$, the origin of the coordinate system; thus they are geodetic lines or surfaces, respectively.

Geometrical objects of $\mathbb{S}^3 \subset \mathbb{H}$ (3)

The orientation distances between

the quaternion x and the axis $B(a_4)$

$$\cos^2 \frac{\omega_b}{2} = (\mathrm{Sc}(a_4^* x))^2 = 1 - (\mathrm{Sc}(a_3^* x))^2 - (\mathrm{Sc}(a_2^* x))^2 - (\mathrm{Sc}(a_1^* x))^2 \,,$$

the quaternion x and the circle $C(a_3, a_4)$

$$\cos^2 \frac{\omega_c}{2} = (\mathrm{Sc}(a_4^* x))^2 + (\mathrm{Sc}(a_3^* x))^2 = 1 - (\mathrm{Sc}(a_2^* x))^2 - (\mathrm{Sc}(a_1^* x))^2 \,,$$

the quaternion x and the sphere $S(a_2, a_3, a_4)$

$$\cos^2 \frac{\omega_s}{2} = (\mathrm{Sc}(a_4^* x))^2 + (\mathrm{Sc}(a_3^* x))^2 + (\mathrm{Sc}(a_2^* x))^2 = 1 - (\mathrm{Sc}(a_1^* x))^2 \,.$$

Geometrical objects of $\mathbb{S}^3 \subset \mathbb{H}$ (4)

2d torus of $\mathbb{S}^3$

The spherical torus

$$Q(a_3, a_4; \Theta) = \{ q(r,t) \in \mathbb{S}^3 \,|\, q(s,t) = q_{34}(r) \cos \frac{\Theta}{2} + q_{12}(t) \sin \frac{\Theta}{2} \,, \quad q_{12}(t) \in C(a_1, a_2), \;\; q_{34}(r) \in C(a_3, a_4), \;\; r, t \in [0, 2\pi) \}$$

with radius $\Theta \in [0, \pi]$ contains all quaternions with constant orientation distance Θ to $C(a_3, a_4)$ (and $\pi - \Theta$ to $C(a_1, a_2)$).

For $\Theta = 0$ or π the spherical torus degenerates to the circles $C(a_3, a_4)$ or $C(a_1, a_2)$, respectively.

Geometrical objects of $\mathbb{S}^3 \subset \mathbb{H}$ (5)

2d sphere of $\mathbb{S}^3$

The "small sphere" on $\mathbb{S}^3$ with radius $\Theta \in [0, \pi]$ (in analogy to small circles on $\mathbb{S}^2$)

$$P(a_4; \Theta) = \{ q(s,t) \in \mathbb{S}^3 \,|\, q(s,t) = \pm a_4 \cos \frac{\Theta}{2} + q_{123}(s,t) \sin \frac{\Theta}{2} \,, \quad q_{123}(s,t) \in S(a_1, a_2, a_3), \;\; s \in [0, \pi], \; t \in [0, 2\pi) \}$$

contains all quaternions with constant orientation distance Θ to $B(a_4)$ (and $\pi - \Theta$ to $S(a_1, a_2, a_3)$).

For $\Theta = 0$ or π the small sphere degenerates to the single quaternion $\pm a_4$ or to the sphere $S(a_1, a_2, a_3)$, respectively.

Special cases of rotationally invariant Bingham distributions (1)

Special cases of the Bingham distribution may be distinguished according to the dimension of their set of modes and related to "Ideal–Lagen", as introduced by Grewen and Wassermann.

The sets of modes are

- $M_b(x) = B(a_4)$ in the bipolar case,
- $M_c(x) = C(a_3, a_4)$ in the circular case,
- $M_s(x) = S(a_2, a_3, a_4)$ in the spherical case, and
- $M_u(x) = \mathbb{S}^3$ in the uniform case.

Special cases of rotationally invariant Bingham distributions (2)

Bipolar "unimodal" standard orientation density function

$$\begin{aligned} f_b(\omega_b; S_b) &= C_b^{-1}(S_b)\, \exp\left(S_b \cos \omega_b\right) [\, ds_3(\omega_b)\,], \\ (\mathcal{R} f_b)(\mathbf{h},\mathbf{r}) &= C_b^{-1}(S_b)\, \exp\!\left(\frac{S_b}{2}\,(z_4 - 1)\right)\, I_0\!\left(\frac{S_b}{2}(1+z_4)\right), \\ & \quad z_4 = a_4\,\mathbf{h}\, a_4^* \cdot \mathbf{r}. \end{aligned}$$

Circular "fibre" standard orientation density function

$$\begin{aligned} f_c(\omega_c;\ S_c) &= C_c^{-1}(S_c)\, \exp(\, S_c\ \cos\omega_c\,)\, [ds_3(\omega_{\mathbf{c}})], \\ (\mathcal{R} f_c)(\mathbf{h},\mathbf{r}) &= C_c^{-1}(S_c)\, \exp\left(\, S_c\, z_h\, z_r\,\right)\, I_0\Big(\, S_c\, \sqrt{1-z_h^2}\,\sqrt{1-z_r^2}\,\Big), \\ & \quad z_h = \mathbf{h}\cdot\mathbf{h}_0,\ z_r = \mathbf{r}\cdot\mathbf{r}_0. \end{aligned}$$

Special cases of rotationally invariant Bingham distributions (3)

Spherical "surface" standard orientation density function

$$\begin{aligned} f_s(\omega_s; S_s) &= C_s^{-1}(S_s)\, \exp\left(S_s \cos \omega_s\right) [\, ds_3(\omega_s)\,], \\ (\mathcal{R} f_s)(\mathbf{h},\mathbf{r}) &= C_s^{-1}(S_s)\, \exp\!\left(\frac{S_s}{2}\,(1 - z_1)\right)\, I_0\!\left(\frac{S_s}{2}(1+z_1)\right), \\ & \quad z_1 = a_1\,\mathbf{h}\, a_1^* \cdot \mathbf{r}. \end{aligned}$$

Generalization, the crystallographic exponential family CEF

The crystallographic exponential family CEF $(g; L, \overset{:}{G}, \dot{G}, \theta)$ introduced by van den Boogaart as

$$f(g;\theta) = A(\theta)\exp\left(-\sum_{\ell=1}^{L}\sum_{\mu,\nu}\theta_\ell^{\mu\nu}\, T_\ell^{\mu\nu}(g)\right)$$

is characterized by

- a maximum order L of series expansion of the potential function into generalized spherical harmonics $T_\ell^{\mu\nu}$,
- a crystal symmetry group $\overset{:}{G}$,
- a specimen symmetry group $\dot{G}$,
- a parameter vector θ, and
- a normalization constant $A^{-1}(\theta)$.

Crystal and sample symmetries are assumed to be triclinic in the following, i.e. CEF $(g; L, C_1, C_1, \theta)$ is analyzed.

Crystallographic exponential family CEF

Van den Boogaart provided the form of parameters θ, for which the elements of CEF represent the special cases of unimodal and fibre textures.

A parameter set of the form $\theta_\ell^{\mu\nu} = -a_\ell T_\ell^{\mu\nu}(g_0)$ results in the rotationally invariant elements of spherical type given by

$$\begin{aligned} f_s(g;\mathbf{a}) &= A_s(\mathbf{a})\exp\left(\sum_{\ell=1}^{L} a_\ell\ \mathrm{tr}(\,T_\ell(gg_0^{-1}))\right) \\ &= A_s(\mathbf{a})\exp\left(\sum_{\ell=1}^{L} a_\ell\ \frac{\sin((2l+1)\frac{\omega_b}{2})}{\sin\frac{\omega_b}{2}}\right), \end{aligned}$$

where ω_b denotes the orientation distance $\omega(gg_0^{-1})$. It is unimodal with mode g_0 if $a_\ell > 0,\ \ell = 0,\dots,L$, and it is multimodal with respect to the orthogonally complementary sphere $g_0^\perp$ of g_0 if $a_\ell < 0,\ \ell = 0,\dots,L$.

Crystallographic exponential family $\mathbb{CEF}$

A parameter set of the form $\theta_\ell^{\mu\nu} = -a_\ell Y_\ell^\mu(\mathbf{h}_0) Y_\ell^\nu(\mathbf{r}_0)$ results in the rotationally invariant elements of circular type given by

$$\begin{aligned} f_c(g;\mathbf{a}) &= A_c(\mathbf{a}) \exp\Big(\sum_{\ell=1}^{L} a_\ell \sum_{\mu,\nu} Y_\ell^\mu(\mathbf{h}_0) T_\ell^{\mu\nu}(g) Y_\ell^\nu(\mathbf{r}_0) \Big) \\ &= A_c(\mathbf{a}) \exp\Big(\sum_{\ell=1}^{L} a_\ell \, \frac{2\ell+1}{4\pi} \, P_\ell(\cos\omega_c) \Big), \end{aligned}$$

which depend only on the orientation distance $\omega_c = \arccos(\mathbf{r}_0 \cdot g \cdot \mathbf{h}_0)$ between g and the circle of orientations mapping $\mathbf{h}_0$ onto $\mathbf{r}_0$.

The distribution corresponds to a $(\mathbf{h}_0, \mathbf{r}_0)$–fibre texture if $a_\ell > 0$, $\ell = 0, \ldots, L$, and to a $(\mathbf{h}_0, -\mathbf{r}_0)$–fibre if $a_\ell < 0$, ℓ odd, $\ell = 0, \ldots, L$.

$\mathbb{CEF}$ of first order: von Mises–Fisher or Bingham distribution

The most simple special case $\mathbb{CEF}$ $(g; L = 1, C_1, C_1, \theta)$

$$f_1(g;\theta) = A_1(\theta) \exp\Big(- \sum_{\mu,\nu=1}^{3} \theta_1^{\mu\nu} T_1^{\mu\nu}(g) \Big) = A_1(\theta) \exp\Big(\operatorname{tr}\,(FX^t) \Big)$$

is the von Mises–Fisher matrix distribution equivalent to the Bingham quaternion distribution, since $T_1^{\mu\nu}$ are just the entries of a 3×3 matrix X representing g, and the parameters $-\theta_1^{\mu\nu} = F_{\mu,\nu}$ can be arranged in a 3×3 parameter matrix F.
The rotationally invariant cases result from

- unimodal: $\theta_1^{\mu\nu} = -S_b \, T_1^{\mu\nu}(g_0)$ giving a unimodal standard distribution with mode g_0,
- circular: $\theta_1^{\mu\nu} = -S_c \, (\mathbf{r}_0 \mathbf{h}_0^t)_{\mu\nu}$ giving a $(\mathbf{h}_0, \mathbf{r}_0)$–fibre standard distribution,
- spherical: $\theta_1^{\mu\nu} = S_s \, T_1^{\mu\nu}(g_0)$ giving a surface standard distribution with mode $g_0^\perp$

with some dispersion parameters $S_b, S_c, S_s \geq 0$.

$\mathbb{CEF}$ of second order: cone and ring fibre textures

If the orientation density function describing a given texture is not maximum at any of the sets of a bimodal point, a circle or a sphere (denoted above by B, C, S), but at a certain (constant) distance Θ to one of them, then it cannot be represented by a Bingham distribution. The corresponding modal sets of quaternions are the small sphere $P(a_4; \Theta)$ and the spherical torus $Q(a_3, a_4; \Theta)$. Distributions with mode on the spherical torus are of particular interest, as they correspond to "cone fibre" textures (including the special case of "ring fibre" textures for $\Theta = \pi/2$) as defined by Grewen and Wassermann.

$\mathbb{CEF}$ of second order: cone and ring fibre textures

The rotationally invariant element of $\mathbb{CEF}$ $(g; L = 2, C_1, C_1, \theta)$ of spherical type is given by

$$f_{2,s}(g;\mathbf{a}) = A_{2,s}(\mathbf{a}) \exp\left(a_1(1 + 2\cos\omega_b) + a_2(1 + 2\cos\omega_b + 2\cos(2\omega_b)) \right).$$

It contains all transitional cases from bipolar over small sphere to spherical distributions with mode at g_0, on the small sphere centered at g_0 with radius $\Theta = \arccos \frac{-a_1 - a_2}{4a_2}$ (for $|\frac{-a_1-a_2}{4a_2}| \leq 1$) or at $g_0^\perp$, respectively.

For $a_2 = 0$, the distribution $f_{2,s}$ resembles the rotationally invariant bipolar ($a_1 > 0$) or spherical ($a_1 < 0$) cases of the Bingham distribution.

$\mathcal{CEF}$ of second order: cone and ring fibre textures

The rotationally invariant element of $\mathcal{CEF}$ $(g; L = 2, C_1, C_1, \theta)$ of circular type is given by

$$f_{2,c}(g; \mathbf{a}) = A_{2,c}(\mathbf{a}) \exp\left(a_1 \cos\omega_c + \frac{5a_2}{12}(1 + 3\cos(2\omega_c))\right) .$$

It contains all transitional cases from fibre over cone to ring over anti–cone to anti–fibre textures. The modal set is the spherical torus around the circle given by $(\mathbf{h}_0, \mathbf{r}_0)$ with radius $\Theta = \arccos \frac{-a_1}{5a_2}$ (for $|\frac{-a_1}{5a_2}| \leq 1$), otherwise it is the circle $(\mathbf{h}_0, \mathbf{r}_0)$ or its complement $(-\mathbf{h}_0, \mathbf{r}_0)$ themselves. A ring fibre texture is formed if $a_1 = 0$ and $a_2 > 0$ $(\Theta = \pi/2)$, which has its mode at equal distance to both complementary circles. A "double fire–tree" fibre texture results from $a_1 = 0$ and $a_2 < 0$, where both circles are equally occupied modes. For $a_2 = 0$, the distribution $f_{2,c}$ resembles the rotationally invariant (circular) cases of the Bingham distribution with respect to the $(\mathbf{h}_0, \mathbf{r}_0)$–fibre for $a_1 > 0$, and to the $(-\mathbf{h}_0, \mathbf{r}_0)$–fibre for $a_1 < 0$.

Conclusions

Special cases of the Bingham quaternion distribution represent rotationally invariant distributions around "Ideallagen" of polar, fibre, and surface texture type, including continuous transitions between those end members.
They correspond to first order elements of the crystallographic exponential family.

The rotationally invariant second order elements of circular type have their modes on the spherical torus and represent cone and ring fibre textures.

The MTEX Project

Statistical analysis of EBSD data from individual crystallites

Statistical analysis of EBSD data from individual crystallites with MTEX

Contents

- **Motivation and introduction**
- **Statistical analysis of orientation data**
- **Practical application to simulated data**
- **Practical application to experimental data**
- **Conclusions**

Texture Analysis with MTEX

Motivation and Introduction

Motivation and introduction

EBSD data and the definiton of "grains"

Crystal grains are defined, not detected, with spatially indexed EBSD measurements using a threshold δ.

Then measurements are assigned to grains, resulting in subsamples of 1000s of measurements per grain.

Depending on

- experimental errors,
- the very definition, i.e., the threshold δ, and
- internal defects of the grains

the orientation distribution per grain is usually highly concentrated.

Statistics per grain

Orientation statistics aids to the distinction of several types of highly concentrated orientation distributions, where the notation is borrowed from special symmetrical cases of the Bingham distribution on $\mathbb{S}^3 \subset \mathbb{R}^4$.

Texture Analysis with MTEX

Statistical analysis of orientation data

Orientations, rotations, and quaternions

The rotational group $SO(3)$ may be considered in terms of $\mathbb{H}$, the skew field of real quaternions. In particular, a unit quaternion $q \in \mathbb{S}^3 \subset \mathbb{H}$ determines a rotation.

The unit quaternion q and its negative $-q$ define the same rotation. Thus, it would make sense to identify the pair $(q, -q)$ with a unique rotation; the proper entity to work with is the (4×4) symmetric matrix

$$Q = \begin{pmatrix} q_1^2 & q_1 q_2 & q_1 q_3 & q_1 q_4 \\ q_1 q_2 & q_2^2 & q_2 q_3 & q_2 q_4 \\ q_1 q_3 & q_2 q_3 & q_3^2 & q_3 q_4 \\ q_1 q_4 & q_2 q_4 & q_3 q_4 & q_4^2 \end{pmatrix}.$$

Thinking of $q = (q_1, q_2, q_3, q_4)^\mathsf{T}$ as elements of $\mathbb{S}^3 \subset \mathbb{R}^4$ we could write $Q = qq^\mathsf{T}$.

Orientation statistics (1)

Orientation tensor

Given orientation data $q_\ell = q(x_\ell), q_\ell \in \mathbb{S}^3, x_\ell \in \mathbb{R}^2, \ell = 1, \ldots, n$, the key (non-spatial) summary statistic is the orientation tensor

$$T = \frac{1}{n}\sum_{\ell=1}^{n} Q_\ell = \frac{1}{n}\sum_{\ell=1}^{n} q_\ell q_\ell^{\mathsf{T}}.$$

Its spectral decomposition into the set of eigenvectors (quaternions) $a_1, \ldots, a_4 \in \mathbb{S}^3$ and the set of corresponding real eigenvalues $\lambda_1, \ldots, \lambda_4$ provides a measure of location and a corresponding measure of dispersion, respectively.

Shape parameters of the Bingham quaternion distribution

If the data are sampled from a Bingham population, then the eigenvalues λ_i are related to the shape parameters κ_i, $i = 1, \ldots, 4$, of the Bingham (quaternion) distribution by a system of algebraic equations involving partial derivatives of the confluent hypergeometric function ${}_1F_1$ of a (4×4) matrix argument.

Orientation statistics (2)

Tensor of inertia

Since the orientation tensor T and the tensor of inertia I are related by

$$I = E - T,$$

where E denotes the unit matrix, the eigenvectors of T provide the principal axes of inertia and the eigenvalues of T provide the principal moments of inertia.

Bingham quaternion distribution (1)

General case

Neglecting the spatial dependence of EBSD data from a single crystalline grain, the Bingham quaternion distribution

$$\begin{aligned} f(\pm q; A) &= \left({}_1F_1(\tfrac{1}{2}, 2, A)\right)^{-1} \exp\left(q^{\mathsf{T}} A q\right) \\ &= \left({}_1F_1(\tfrac{1}{2}, 2, A)\right)^{-1} \exp\left(\sum_{i=1}^{4} \kappa_i \, (a_i^{\mathsf{T}} q)^2\right) \end{aligned}$$

with shape parameters $\kappa_i \in \mathbb{R}$ with respect to orthonormal $a_i \in \mathbb{S}^3$, $i = 1, \ldots, 4$, and with the hypergeometric function ${}_1F_1(\frac{1}{2}, 2, \circ)$ of matrix argument seems appropriate.
It is emphasized that the densities $f(\pm q; A)$ and $f(\pm q; A + tE)$, with $t \in \mathbb{R}$ and the (4×4) identity matrix E, define the same distribution.

Sepcial cases of Bingham quaternion distribution (1)

Spherically symmetric bimodal Watson distribution, $\kappa > 0$

$$\begin{aligned} f(\pm q; A) &= \left({}_1F_1(\tfrac{1}{2}, 2, A)\right)^{-1} \exp\left(\kappa \, (a^{\mathsf{T}} q)^2\right) \\ &= \left({}_1F_1(\tfrac{1}{2}, 2, A)\right)^{-1} \exp\left(\kappa \, \cos^2(\angle(a, q))\right) \end{aligned}$$

with mode at $\pm a$.

Fibre Bingham distribution, $\kappa > 0$

$$f(\pm q; A) = \left({}_1F_1(\tfrac{1}{2}, 2, A)\right)^{-1} \exp\left(\kappa \, ((a_1^{\mathsf{T}} q)^2 + (a_2^{\mathsf{T}} q)^2)\right)$$

with modes along the great circle spanned by a_1 and a_2 mapping the crystallographic direction $h = a_1^* a_2$ on the specimen direction $r = a_2 a_1^*$.

Sepcial cases of Bingham quaternion distribution (2)

Oblate bimodal Bingham distribution, $\kappa_1 \gg \kappa > 0$

$$f(\pm q; A) = \Big({}_1F_1(\frac{1}{2}, 2, A)\Big)^{-1} \exp\big(\kappa_1\ (a_1^\mathsf{T} q)^2 + \kappa\ ((a_2^\mathsf{T} q)^2 + (a_3^\mathsf{T} q)^2)\big)$$

with mode at $\pm a$.

Prolate bimodal Bingham distribution, $\kappa_1 \gg \kappa_2 > \kappa > 0$

$$f(\pm q; A) = \Big({}_1F_1(\frac{1}{2}, 2, A)\Big)^{-1} \exp\big(\kappa_1\ (a_1^\mathsf{T} q)^2 + \kappa_2\ (a_2^\mathsf{T} q)^2 + \kappa\ ((a_3^\mathsf{T} q)^2 + (a_4^\mathsf{T} q)^2)\big)$$

with mode at $\pm a$.

Bingham quaternion distribution (3)

Maximum likelihood estimates

The estimates of the parameters of the Bingham quaternion distribution based on the sample $q_1, \dots, q_n$ are given by

$$\widehat{U} = V^\mathsf{T}, \tag{29}$$

$$\frac{\partial \log\, {}_1F_1(\frac{1}{2}, 2, K)}{\partial \kappa_i}\Big|_{K=\widehat{K}} = \lambda_i, \quad i = 1, \dots, 4. \tag{30}$$

It should be noted that Eq. (30) determines $\widehat{\kappa}_i, i = 1, \dots, 4$, only up to an additive constant, because $\widehat{\kappa}_i$ and $\widehat{\kappa}_i + t, i = 1, \dots, 4$, result in the same $\lambda_i, i = 1, \dots, 4$. Uniqueness could be conventionally imposed by setting $\widehat{\kappa}_4 = 0$.

Large concentration asymptotics

Provided that $\kappa_1 \gg \kappa_2, \kappa_3, \kappa_4$

$$\kappa_j - \kappa_1 \simeq -(2\lambda_j)^{-1}. \tag{31}$$

Bingham quaternion distribution (5)

Spherical shape

Since we expect that κ_1 and $\widehat{\kappa}_1$ are very large, the interesting statistical issue is to test rotational symmetry, i.e., to test the null hypothesis of

- spherical symmetry that $\kappa_2 = \kappa_3 = \kappa_4$.

Oblate and prolate shape

If this hypothesis can be rejected we would be interested in distinguishing

- "prolate" symmetry $\kappa_2 > \kappa_3 = \kappa_4$, and
- "oblate" symmetry $\kappa_2 = \kappa_3 > \kappa_4$, respectively.

Bingham quaternion distribution (6)

Spherical shape

Assuming rotational symmetry, i.e., degeneracy of the Bingham to the Watson distribution, the test statistic

$$T_s^{\text{Bingham}} = n \sum_{\ell=2}^{4} (\widehat{\kappa}_\ell - \bar{\kappa})(\lambda_\ell - \bar{\lambda}) \sim \chi_5^2, n \to \infty, \tag{32}$$

where

$$\bar{\kappa} = \frac{1}{3} \sum_{\ell=2}^{4} \widehat{\kappa}_\ell, \quad \bar{\lambda} = \frac{1}{3} \sum_{\ell=2}^{4} \lambda_\ell.$$

For a given sample of individual orientation measurements $q_1, \dots, q_n$ we compute the value t_s and the corresponding

$$p = \mathrm{Prob}(T_s > t_s),$$

and conclude that the null hypothesis of rotational symmetry may be rejected for any significance level $\alpha > p$.

Bingham quaternion distribution (7)

Oblate and prolate case

If the hypothesis of spherical symmetry is rejected, we test for the prolateness using

$$T_p^{\text{Bingham}} = \frac{n}{2}(\widehat{\kappa}_3 - \widehat{\kappa}_4)(\lambda_3 - \lambda_4) \sim \chi_2^2, n \to \infty, \tag{33}$$

or, analogously, for the oblateness using

$$T_o^{\text{Bingham}} = \frac{n}{2}(\widehat{\kappa}_2 - \widehat{\kappa}_3)(\lambda_2 - \lambda_3) \sim \chi_2^2, n \to \infty, \tag{34}$$

respectively.

Bingham quaternion distribution (8)

According to Eq. (31), for $1 \approx \lambda_1 >> \lambda_2 \geq \lambda_3 \geq \lambda_4$ we may apply the asymptotics

$$\kappa_j \simeq \widetilde{\kappa_j} = -(2\lambda_j)^{-1} \quad (j = 2, 3, 4), \tag{35}$$

assuming $\kappa_1 \simeq \widetilde{\kappa_1} = 0$. Then the test statistics T^{Bingham} simplify to

$$T_s^{\text{Bingham}} \simeq T_s^{\text{asymp Bingham}} = \frac{n}{6} \sum_{i=2,3,4} \sum_{j=2,3,4} \left(\frac{\lambda_i}{\lambda_j} - 1 \right) \tag{36}$$

$$T_p^{\text{Bingham}} \simeq T_p^{\text{asymp Bingham}} = \frac{n}{4} \left(\frac{\lambda_3}{\lambda_4} + \frac{\lambda_4}{\lambda_3} - 2 \right) \tag{37}$$

$$T_o^{\text{Bingham}} \simeq T_o^{\text{asymp Bingham}} = \frac{n}{4} \left(\frac{\lambda_2}{\lambda_3} + \frac{\lambda_3}{\lambda_2} - 2 \right). \tag{38}$$

Note that three summands in Eq. (36) vanish and that the λ_j are arranged in decreasing order. These formulas agree well with the common sense interpretation of a spherical, prolate and oblate shape, respectively.

Inferential statistics without parametric assumptions (1)

Second moments

Dropping the assumption that $\pm q$ has a Bingham distribution and applying large sample approximation, only

$$c_{ij} = \frac{1}{n} \sum_{\ell=1}^{n} (q_\ell^{\mathsf{T}} a_i)^2 (q_\ell^{\mathsf{T}} a_j)^2, i, j = 1, \ldots, 4,$$

is required, where a_i are the eigenvectors of T corresponding to eigenvalues $\lambda_i, i = 1, \ldots, 4$.

Inferential statistics without parametric assumptions (2)

Non-parametric test statistics

Then the test statistics are
for the spherical case

$$T_s = 15n \frac{\lambda_2^2 + \lambda_3^2 + \lambda_4^2 - (1 - \lambda_1)^2)/3}{2(1 - 2\lambda_1 + c_{11})} \sim \chi_5^2, n \to \infty, \tag{39}$$

for the prolate case

$$T_p = 8n \frac{\lambda_3^2 + \lambda_4^2 + (1 - \lambda_1 - \lambda_2)^2/2}{2(1 - 2(\lambda_1 + \lambda_2) + c_{11} + 2c_{12} + c_{22})} \sim \chi_2^2, n \to \infty, \tag{40}$$

and for the oblate case

$$T_o = 8n \frac{\lambda_2^2 + \lambda_3^2 + (1 - \lambda_1 - \lambda_4)^2/2}{2(1 - 2(\lambda_1 + \lambda_4) + c_{11} + 2c_{14} + c_{44})} \sim \chi_2^2, n \to \infty. \tag{41}$$

Texture Analysis with MTEX

Practical application to simulated data

Orientation maps of simulated data (1a)

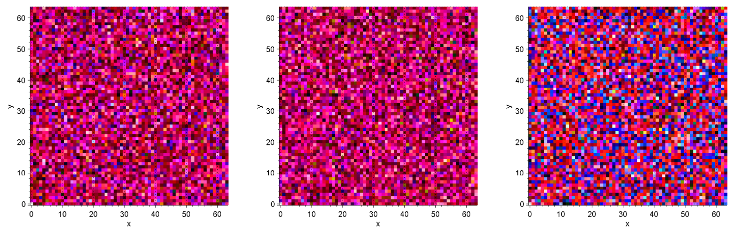

$(400, 190, 190, 0)$ $(340, 0, 0, 0)$ $(210, 190, 0, 0)$

64×64 simulated spatially indexed individual orientations according to Bingham quaternion distribution with shape parameters $(400, 190, 190, 0)$, $(340, 0, 0, 0)$, $(210, 190, 0, 0)$;
RGB colour coding of Bunge's Euler angles $(\varphi_1, \phi, \varphi_2)$ according to (zxz) convention associating φ_1 with red, ϕ with green, and φ_2 with blue.

Orientation maps of simulated data (1b)

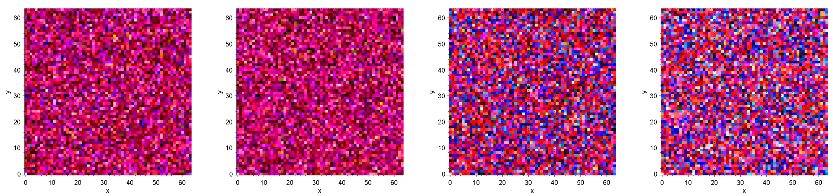

$(400, 190, 190, 0)$ $(340, 0, 0, 0)$ $(210, 190, 0, 0)$ $(200, 200, 0, 0)$

64×64 simulated spatially indexed individual orientations according to Bingham quaternion distribution with shape parameters $(400, 190, 190, 0)$, $(340, 0, 0, 0)$, $(210, 190, 0, 0)$, and $(200, 200, 0, 0)$;
RGB colour coding of Bunge's Euler angles $(\varphi_1, \phi, \varphi_2)$ according to (zxz) convention associating φ_1 with red, ϕ with green, and φ_2 with blue.

3d axis-angle scatter plots of simulated data (2a)

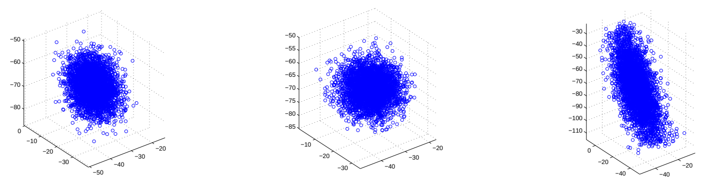

$(400, 190, 190, 0)$ $(340, 0, 0, 0)$ $(210, 190, 0, 0)$

4096 simulated spatially indexed individual orientations according to Bingham quaternion distribution with shape parameters $(400, 190, 190, 0)$, $(340, 0, 0, 0)$, $(210, 190, 0, 0)$.

3d axis-angle scatter plots of simulated data (2b)

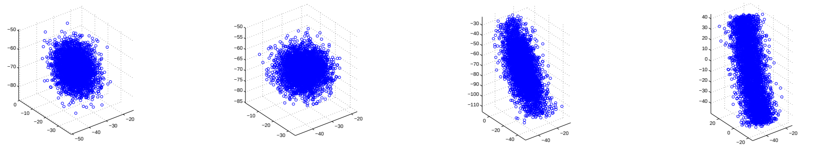

(400, 190, 190, 0) (340, 0, 0, 0) (210, 190, 0, 0) (200, 200, 0, 0)

4096 simulated spatially indexed individual orientations according to Bingham quaternion distribution with shape parameters (400, 190, 190, 0), (340, 0, 0, 0), (210, 190, 0, 0), and (200, 200, 0, 0).

Centered 3d axis-angle scatter plots of simulated data (2c)

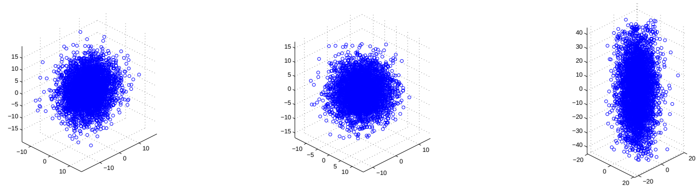

(400, 190, 190, 0) (340, 0, 0, 0) (210, 190, 0, 0)

4096 simulated spatially indexed individual orientations according to Bingham quaternion distribution with shape parameters (400, 190, 190, 0), (340, 0, 0, 0), (210, 190, 0, 0).

Centered 3d axis-angle scatter plots of simulated data (2d)

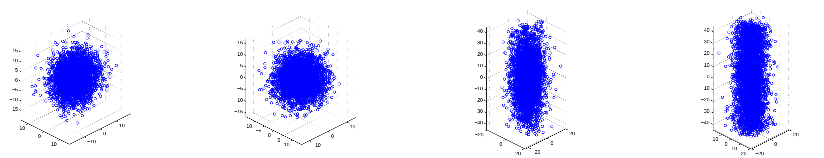

(400, 190, 190, 0) (340, 0, 0, 0) (210, 190, 0, 0) (200, 200, 0, 0)

4096 simulated spatially indexed individual orientations according to Bingham quaternion distribution with shape parameters (400, 190, 190, 0), (340, 0, 0, 0), (210, 190, 0, 0), and (200, 200, 0, 0).

Pole point plots of simulated data (4a)

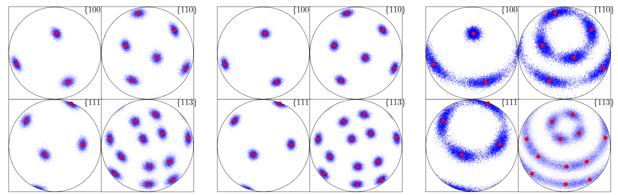

(400, 190, 190, 0) (340, 0, 0, 0) (210, 190, 0, 0)

(100), (110), (111), and (311) pole point plots of 4096 simulated spatially indexed individual orientations according to Bingham quaternion distribution with shape parameters (400, 190, 190, 0), (340, 0, 0, 0), (210, 190, 0, 0).

Pole point plots of simulated data (4b)

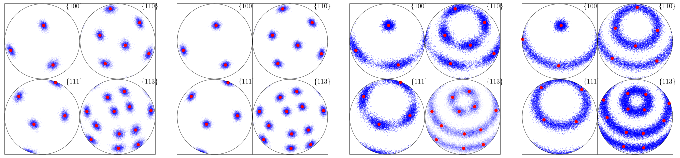

$(400, 190, 190, 0)$ $(340, 0, 0, 0)$ $(210, 190, 0, 0)$ $(200, 200, 0, 0)$

$(100), (110), (111)$, and (311) pole point plots of 4096 simulated spatially indexed individual orientations according to Bingham quaternion distribution with shape parameters $(400, 190, 190, 0)$, $(340, 0, 0, 0)$, $(210, 190, 0, 0)$, and $(200, 200, 0, 0)$.

σ-plots of odfs of simulated data (5a)

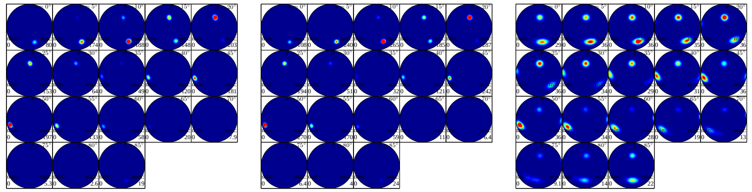

$(400, 190, 190, 0)$ $(340, 0, 0, 0)$ $(210, 190, 0, 0)$

De la Vallée Poussin kernel–estimated ODF of 4096 simulated spatially indexed individual orientations according to Bingham quaternion distribution with shape parameters $(400, 190, 190, 0)$, $(340, 0, 0, 0)$, $(210, 190, 0, 0)$.

σ-plots of odfs of simulated data (5b)

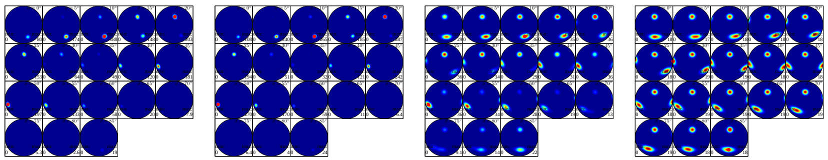

$(400, 190, 190, 0)$ $(340, 0, 0, 0)$ $(210, 190, 0, 0)$ $(200, 200, 0, 0)$

De la Vallée Poussin kernel–estimated ODF of 4096 simulated spatially indexed individual orientations according to Bingham quaternion distribution with shape parameters $(400, 190, 190, 0)$, $(340, 0, 0, 0)$, $(210, 190, 0, 0)$, and $(200, 200, 0, 0)$.

Descriptive statistics: Eigenwerte and shape parameters

Eigenvalues λ_i of T, corresponding shape parameters κ_i of Bingham distribution

	bimodal Bingham $(400, 190, 190, 0)$	bimodal Bingham $(340, 0, 0, 0)$	bimodal Bingham $(210, 190, 0, 0)$	fibre Bingham $(200, 200, 0, 0)$
sample size	4096	4096	4096	4096
texture index	75.2252	101.377	13.4198	9.1839
entropy	-3.8385	-4.1432	-2.1579	-1.8906
λ_1	0.99405	0.99559	0.97021	0.94584
λ_2	0.00239	0.00154	0.02494	0.04909
λ_3	0.00233	0.00147	0.00247	0.00254
λ_4	0.00122	0.00143	0.00237	0.00253
λ_2/λ_3	1.0279	1.0614	10.0899	19.2927
λ_3/λ_4	1.9041	1.0106	1.0411	1.0071
visual inspection	"oblate"	"spherical"	"prolate"	"fibre"
computation applying large concentration approximation, Eq. (35)				
κ_1	408.7925	349.3848	210.5513	197.9093
κ_2	199.9176	23.6685	190.5070	187.7238
κ_3	194.0997	3.6716	8.3073	1.4044
κ_4	0.0000	0.0000	0.0000	0.0000
$\kappa_2 - \kappa_3$	5.8179	19.9969	182.1997	186.3193
$\kappa_3 - \kappa_4$	194.0997	3.6716	8.3073	1.4044

Inferential statistics

Statistical tests				
	bimodal Bingham (400, 190, 190, 0)	bimodal Bingham (340, 0, 0, 0)	bimodal Bingham (210, 190, 0, 0)	fibre Bingham (200, 200, 0, 0)
sample size	4096	4096	4096	4096
Bingham statistics involving large concentration approximation, Eqs. (36), (37), (38)				
$p_{\text{spherical}}$ spherical	0 reject	0.3201 "no rejection"	0 reject	0 reject
p_{oblate} oblate	0.6795 "no rejection"	—	0 reject	0 reject
p_{prolate} prolate	0 reject	—	0.4362 "no rejection"	0.9744 "no rejection"
Large sample approximation statistics without parametric assumptions, Eqs. (39), (40), (41)				
$p_{\text{spherical}}$ spherical	0 reject	0.3077 "no rejection"	0 reject	0 reject
p_{oblate} oblate	0.6805 "no rejection"	—	0 reject	0 reject
p_{prolate} prolate	0 reject	—	0.4461 "no rejection"	0.9745 "no rejection"

Texture Analysis with MTEX

Practical application to experimental data

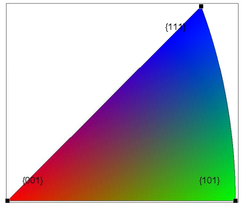

Inverse pole figure colour bar

Individual crystal EBSD data (courtesy W. Pantleon, Risø)

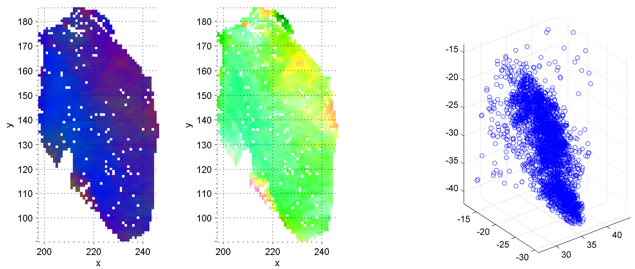

Grain 40 with 3068 spatially indexed individual orientations

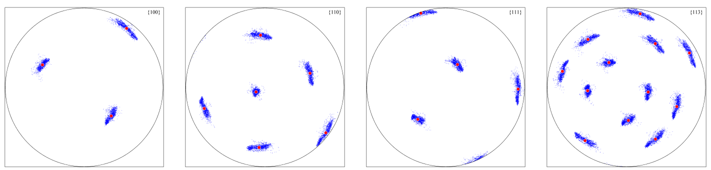

Pole point plots of grain 40 for crystal forms $\{100\}, \{110\}, \{111\}$, and $\{113\}$

Individual crystal EBSD data (courtesy W. Pantleon, Risø)

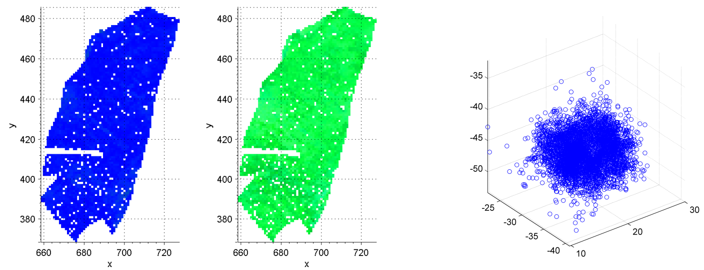

Grain 147 with 4324 spatially indexed individual orientations

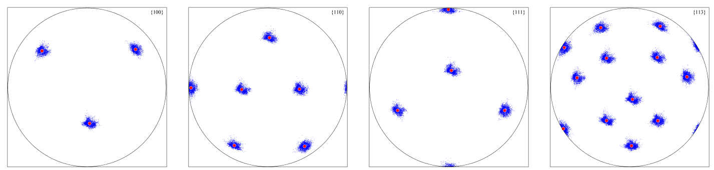

Pole point plots of grain 147 for crystal forms $\{100\}, \{110\}, \{111\}$, and $\{113\}$

Individual crystal EBSD data (courtesy W. Pantleon, Risø)

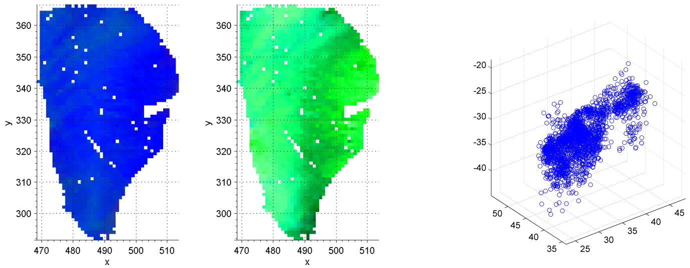

Grain 109 with 2253 spatially indexed individual orientations

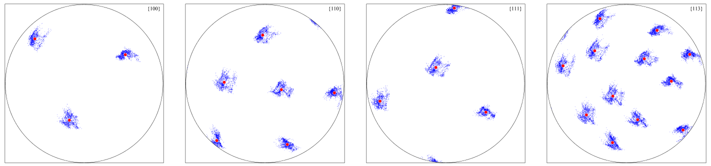

Pole point plots of grain 109 for crystal forms $\{100\}, \{110\}, \{111\}$, and $\{113\}$

Individual crystal EBSD data (courtesy W. Pantleon, Risø)

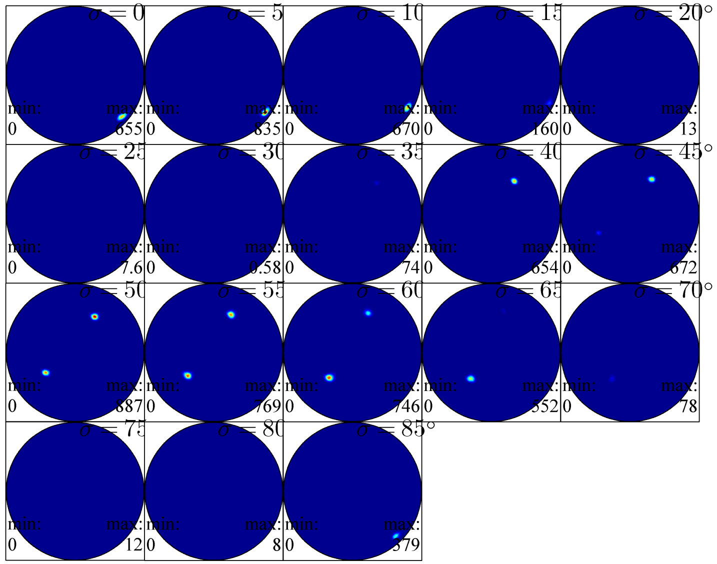

σ–sections of kernel–estimated orientation density of grain 40

Individual crystal EBSD data (courtesy W. Pantleon, Risø)

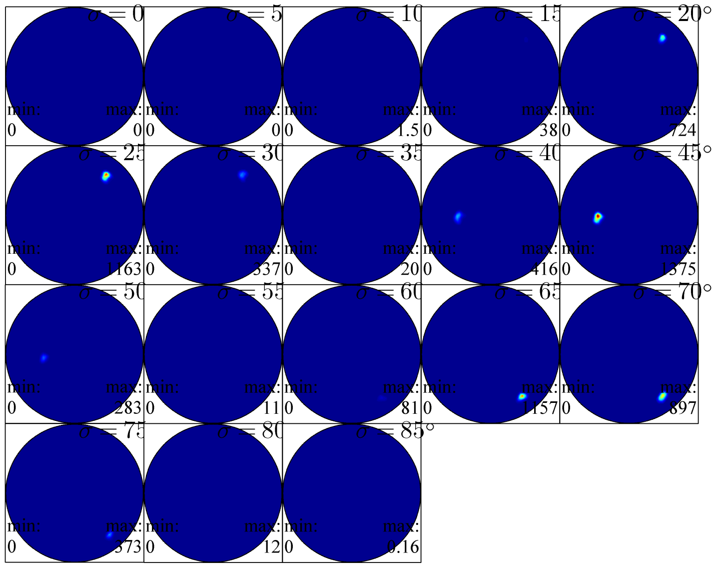

σ–sections of kernel–estimated orientation density of grain 147

Individual crystal EBSD data (courtesy W. Pantleon, Risø)

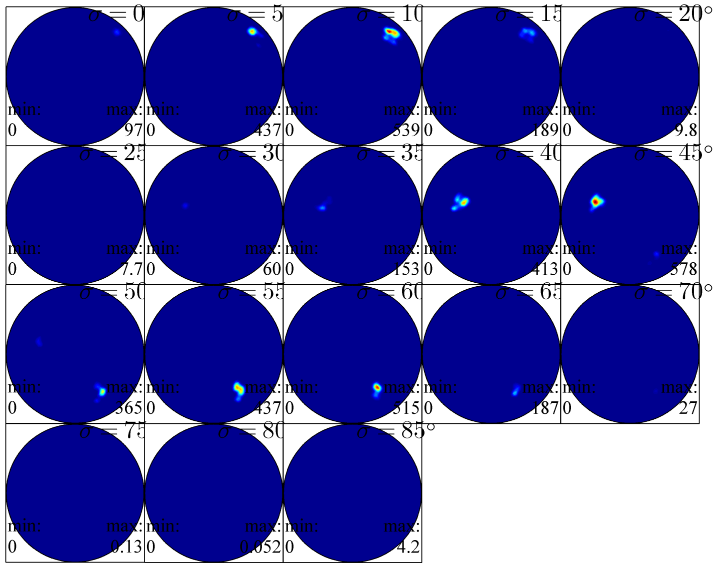

σ–sections of kernel–estimated orientation density of grain 109

Individual crystal EBSD data (courtesy W. Pantleon, Risø)

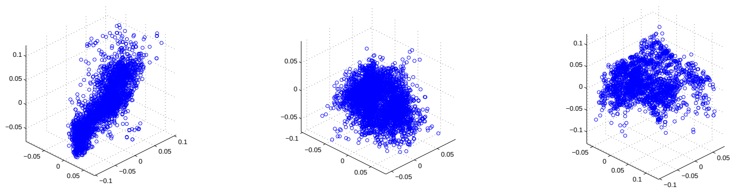

grain 40 | grain 147 | grain 109

Scatter plots in Rodrigues system centered with respect to eigenvector corresponding to largest eigenvalue; grain 40 – "prolate" (left), grain 147 – "spherical" (center), grain 109 – "oblate" (right).

Descriptive statistics: Eigenwerte and shape parameters

Eigenvalues λ_i of T, corresponding shape parameters κ_i of Bingham distribution

	grain 40	grain 147	grain 109
sample size	3068	4324	2253
texture index	337.7395	308.9108	178.4238
entropy	-5.3425	-5.1136	-4.7782
λ_1	0.9965e+000	0.9983e+000	0.9956e+000
λ_2	0.2928e–002	0.8713e–003	0.2166e–002
λ_3	0.3000e–003	0.4989e–003	0.1906e–002
λ_4	0.2645e–003	0.3513e–003	0.3120e–003
λ_2/λ_3	9.7599	1.7465	1.1364
λ_3/λ_4	1.1345	1.4199	6.1100
visual inspection	"prolate"	"spherical"	"oblate"
computation involving ${}_1F_1$, Eq. (30)			
κ_1	1.8908e+003	1.4234e+003	1.6029e+003
κ_2	1.7195e+003	8.4916e+002	1.3716e+003
κ_3	2.2410e+002	4.2083e+002	1.3401e+003
κ_4	0.0	0.0	0.0
$\kappa_2 - \kappa_3$	1.4954e+003	4.2832e+002	31.4763
$\kappa_3 - \kappa_4$	2.2410e+002	4.2083e+002	1.3401e+003
computation applying large concentration approximation, Eq. (35)			
κ_1	1.8903e+003	1.4229e+003	1.6024e+003
κ_2	1.7196e+003	8.4916e+002	1.3716e+003
κ_3	2.2410e+002	4.2083e+002	1.3401e+003
κ_4	0.0	0.0	0.0
$\kappa_2 - \kappa_3$	1.4956e+003	4.2832e+002	31.4763
$\kappa_3 - \kappa_4$	2.2410e+002	4.2083e+002	1.3401e+003

Inferential statistics

Statistical tests

	grain 40	grain 147	grain 109
sample size	3068	4324	2253
Bingham statistics involving ${}_1F_1$, Eqs. (32), (33), (34)			
$p_{spherical}$	0	0	0
spherical	reject	reject	reject
p_{oblate}	0	0	0.0099
oblate	reject	reject	reject for $\alpha > p$
$p_{prolate}$	0.0022	0	0
prolate	reject for $\alpha > p$	reject	reject
Bingham statistics involving large concentration approximation, Eqs. (36), (37), (38)			
$p_{spherical}$	0	0	0
spherical	reject	reject	reject
p_{oblate}	0	0	0.0100
oblate	reject	reject	reject for $\alpha > p$
$p_{prolate}$	0.0022	0	0
prolate	reject for $\alpha > p$	reject	reject
Large sample approximation statistics without parametric assumptions, Eqs. (39), (40), (41)			
$p_{spherical}$	0	0	0
spherical	reject	reject	reject
p_{oblate}	0	0	0.0043
oblate	reject	reject	reject for $\alpha > p$
$p_{prolate}$	0.0418	0	0
prolate	reject for $\alpha > p$	reject	reject

Texture Analysis with MTEX

Conclusions

Conclusions

Given reasonably defined grains and sufficiently many EBSD measurements per grain, it is now possible to analyse them

- in terms of pole and orientation densities, and
- in terms of descriptive and **inferential** statistics.

In particular, we can test for several rotational symmetries, e.g., spherical, oblate and prolate symmetry.
Different symmetries may be indicative of different texture generating processes, e.g., different deformation regimes.

Our novel method as encoded in **MTEX** features a unique approach to analyse integral and individual orientation measurements.